Astronomy & Astrophysics manuscript no. output
May 14, 2026

Asteroseismic forward modelling of 36 β Cep pulsators and inferences on their internal differential rotation

M. Vanrespaille[1], D.J. Fritzewski[1], V. Vanlaer[1], and C. Aerts[1,2,3]

[1] Institute of Astronomy, KU Leuven, Celestijnenlaan 200D, 3001, Leuven, Belgium
e-mail: mathijs.vanrespaille@kuleuven.be
[2] Department of Astrophysics, IMAPP, Radboud University Nijmegen, PO Box 9010, 6500 GL Nijmegen, The Netherlands
[3] Max Planck Institut für Astronomie, Königstuhl 17, 69117 Heidelberg, Germany

ABSTRACT

Context. Asteroseismic observations of the interior rotation of main sequence stars have shown that angular momentum transport is much more efficient than expected. Which transport mechanisms are responsible for this is still unclear. Detections of radial differential rotation provide valuable constraints on these transport mechanisms. This has been detected in several massive main sequence β Cep pulsators, even though fewer than ten β Cep stars have been asteroseismically modelled in detail so far.
Aims. We aim to expand the sample of asteroseismically forward modelled β Cep pulsators to maximally exploit their potential to observationally constrain angular momentum transport mechanisms. To that end, we seek to constrain their rotation profiles.
Methods. We searched for rotational splitting of non-radial modes in a large β Cep sample with identified mode degrees. These were subjected to a novel forward modelling approach, which consistently accounts for second-order rotation effects using the state-of-the-art `StORM` oscillation code.
Results. We successfully modelled 36 β Cep stars and constrained crucial parameters such as their initial mass, internal rotation frequency, convective core mass, and age. Like in intermediate-mass main sequence stars, the internal rotation rate globally decreases in β Cep stars as they evolve along the main sequence. Radial differential rotation is constrained in 17 β Cep stars. The rotation rate in at least 14 stars varies by more than 10%. Of these 14 stars, ten have their rotation rate decreasing from the core to the surface while it is the opposite in four of them.
Conclusions. We affirm that radial differential rotation is common in β Cep stars. Moreover, our constrained rotation profiles suggest that the typical β Cep rotation profile may be non-monotonic.

Key words. Asteroseismology – Stars: oscillations – Stars: massive – Stars: interiors – Stars: evolution – Stars: rotation

1. Introduction

Asteroseismology, the study of pulsating stars, has begun to unveil the interior structure of stars (e.g., Hekker & Christensen-Dalsgaard 2017; García & Ballot 2019; Aerts 2021; Aerts & Tkachenko 2024). Thanks to the recent space photometry revolution brought on by the CoRoT (Auvergne et al. 2009), *Kepler* (Borucki et al. 2010), and TESS (Ricker et al. 2015) telescopes, precise asteroseismic measurements of the interior structure of thousands of stars are now available (see Kurtz 2022, for a recent observational overview). A key goal of asteroseismology is to unravel transport processes inside the stars, notably angular momentum transport mechanisms such as those described by Zahn (1992); Talon et al. (1997); Mathis & Zahn (2004, 2005); Mathis et al. (2013); Rogers et al. (2013). Calibrating these processes requires a measurement of the internal rotation profile of stars in various evolutionary stages (e.g., Deheuvels et al. 2014; Kurtz et al. 2014; Triana et al. 2015; Di Mauro et al. 2016; Triana et al. 2017; Li et al. 2024; Aerts et al. 2019, for a review).

Asteroseismic studies of hundreds of intermediate-mass main sequence stars with a convective core have revealed that the vast majority of them rotate quasi-rigidly regardless of their age (Ouazzani et al. 2019; Li et al. 2020; Aerts 2021, for a review). These observations stand in stark contrast to the predictions of radial differential rotation increasing with age when no angular momentum is transported (e.g., Maeder 2009) or when modelling angular momentum transport by meridional circulation and turbulence (e.g., Zahn 1992; Talon et al. 1997; Decressin et al. 2009; Amard et al. 2019). As such, angular momentum transport in intermediate-mass main sequence stars must be far more efficient than previously thought. It is currently unclear which transport mechanisms are responsible for this efficient angular momentum transport along the main sequence. As a result, current stellar evolution models are subjected to considerable systematic uncertainty. Moreover, these transport mechanisms could also transport material, further affecting the star's structure and evolution. Efficient internal mixing refuels the convective core and thus extends the star's lifetime, smoothens chemical gradients, and brings metals produced in the core to the surface.

Our present study aims to lift our knowledge of the internal rotation properties of high-mass main sequence stars to a population level. The most massive main sequence pulsators are the β Cephei (β Cep) stars. They display low-order pressure-(p-) and gravity-(g-)modes and have masses between approximately 8 and 30 $M_\odot$ (Aerts et al. 2010; Bowman 2020; Kurtz 2022). Unlike intermediate-mass main sequence pulsators, most β Cep pulsators with internal rotation measurements display differential rotation. Such differential rotation was first reported by Aerts et al. (2003) and was recently summarised by Burssens et al. (2023). Hence, β Cep stars provide valuable constraints to angular momentum transport studies in the high-mass regime. However, the exploitation of this pulsator class is limited by the

small number of targets for which the internal rotation rate was measured. Fewer than ten β Cep stars have been asteroseismically modelled in detail and never all together in a consistent population-level study. Of these stars, only five provided constraints on their differential rotation (Burssens et al. 2023). In three stars the rotation rate near the core is up to about 3 times faster than near the surface. In one case, the near-core region rotates slightly slower than the envelope and the final star rotates quasi-rigidly.

CoRoT observed only one genuine β Cep star but it did not reveal any information on its internal rotation (Degroote et al. 2009) and *Kepler* observed none with proper mode identification. This is not surprising given that β Cep pulsators were not the main focus of these space missions. Several hundreds of β Cep stars were recently discovered by TESS (e.g., Shi et al. 2024; Eze & Handler 2024) and other projects (e.g., Burssens et al. 2019; Labadie-Bartz et al. 2020; Pereira et al. 2024). However, the internal rotation profile has only been constrained in one of these stars, namely HD 192575 (Burssens et al. 2023; Vanlaer et al. 2025). This shortage is due to a lack of mode identifications of the detected oscillations, which are necessary to measure the interior rotation rate of β Cep pulsators. The internal rotation is usually measured from rotational splitting of non-radial modes via the Ledoux constant of that splitting (Ledoux 1951). As the low-order modes of β Cep stars do not occur in the asymptotic regimes of low or high frequencies, their Ledoux constants must be extracted from a proper stellar structure model of the star. Such a model is usually found by forward asteroseismic modelling of zonal mode frequencies, whereby the observed frequencies are matched to model predictions. Forward asteroseismic modelling is only reliable if at least a few observed modes are identified (Ausseloos et al. 2004). Moreover, most forward modelling efforts used a first-order perturbative treatment of rotation, which is not optimal for the β Cep frequency regime (Suárez et al. 2009, and references therein).

Mode identification of β Cep pulsations was historically performed from ground-based multi-colour photometry (e.g., Heynderickx et al. 1994) or spectroscopic line profile variations (e.g., Aerts & De Cat 2003). This research was boosted by long-duration multi-site observation campaigns of a few bright β Cep targets (e.g., Handler et al. 2004; Aerts et al. 2004b; Handler et al. 2005; Briquet et al. 2005; Handler et al. 2006, 2012; Briquet et al. 2012). However, these require significant allocations of telescope time, international collaboration efforts, and intricate analyses. Consequently, such campaigns are difficult and expensive to scale up to large samples, especially for dim targets. Despite these challenges, modern ground-based multi-site monitoring projects to identify the signals in a few dozen bright β Cep stars are ongoing, such as the Global Asteroseismology Project (Shitrit & Arcavi 2024).

A new avenue towards β Cep mode identification recently opened up in the form of space-based multi-colour photometry. Hey & Aerts (2024) demonstrated that the sparse time series photometry of the *Gaia* space telescope (Gaia Collaboration et al. 2016, 2023) captures the dominant frequency detected by TESS in over 80% of pulsators with an amplitude above 4 mmag. Subsequently, Fritzewski et al. (2025) performed a multi-colour analysis on over 200 β Cep stars based on their amplitudes in the TESS and *Gaia* passbands. For 143 of these stars, they identified the most likely degree of the dominant mode. In 33 of these stars, they also found a rotationally split multiplet which includes the dominant mode. These multiplets were subsequently matched to stellar models to estimate the envelope rotation rate. *Gaia* spectroscopy placed a lower limit on the surface rotation frequency of 20 of these pulsators. Based on these two rotation frequencies, Fritzewski et al. (2025) provided upper limits on the envelope-to-surface rotation ratio of these 20 stars . These limits vary between 0.3 and 4, albeit with considerable uncertainty.

In this study, we provide observational constraints to future theoretical studies of angular momentum transport in high-mass main sequence stars by bringing β Cep asteroseismology to a population level. To that end, we revisit the sample of Fritzewski et al. (2025) looking for β Cep stars with sufficient mode identifications to asteroseismically model. Our sample of β Cep stars is described in Sect. 2. Section 3 presents a new grid of stellar models and their oscillation predictions. This grid enables a novel asteroseismic modelling approach consistently including second-order rotation effects, as described in Sect. 4. Based on these results, Sect. 5 evaluates the impact of the second-order rotation effects. Section 6 delves into relations between the asteroseismically inferred rotation and stellar parameters. The detections of differential rotation are shown and discussed in Sect. 7. Finally, a summary and our conclusions are presented in Sect. 8.

2. Target selection

The goal of forward asteroseismic modelling is to constrain a number of free parameters and the input physics of stellar models by matching the observed frequencies of identified modes to those predicted by those models. At minimum, this must constrain the stellar mass and age for a chosen initial metallicity and chemical mixture. For intermediate- and high-mass stars, core-boundary mixing (Dupret et al. 2004; Mazumdar et al. 2006; Johnston 2021; Pedersen et al. 2021) and envelope mixing (Moravveji et al. 2015; Pedersen et al. 2021) are also essential ingredients. We seek to evaluate the rotation rate as well, hence our optimisation problem is five-dimensional. Therefore, we aim for five observational constraints to attempt to break the degeneracies between the free parameters. Two such constraints can be provided by the effective temperature and luminosity, which are now available for most known β Cep stars from *Gaia* DR3. The remaining constraints come from observed mode frequencies, for which the azimuthal order of observed modes must be known to account for rotational shifts. Therefore, we require a sample of β Cep stars with at least three observed frequencies with an identified degree and azimuthal order. No sample with these stringent selection requirements on mode identifications has been collected or modelled before.

2.1. Initial input from Fritzewski et al. (2025)

Most of our sample stars are selected from the 222 β Cep stars presented in Fritzewski et al. (2025) and we followed their approach in drawing their stellar parameters from *Gaia*. When available, the effective temperature $T_{\rm eff}$ comes from *Gaia*'s ESP-HS pipeline (Fouesneau et al. 2023). Otherwise, we took $T_{\rm eff}$ from the GSPPHOT-OB pipeline. Following Fritzewski et al. (2025), we took a conservative relative uncertainty of 10% for $T_{\rm eff}$ as the errors listed in *Gaia* DR3 are unrealistically small (Fouesneau et al. 2023). Together with the measurements of distance, mean G magnitude, and extinction from GSPPHOT-OB, these $T_{\rm eff}$ were used to find the luminosity L using Pedersen et al. (2020)'s Model 1 bolometric correction. Finally, like Fritzewski et al. (2025) did, we estimated the surface rotation frequency with an unknown projection factor $f_{\rm rot} \sin i$ for 167 β Cep stars by combining the ESP-HS projected surface velocity with the radius computed from L and $T_{\rm eff}$.

We drew on the TESS light curves, Fourier analyses, and identifications of mode degrees of Fritzewski et al. (2025) as the foundation to build our sample on. By combining *Gaia* and TESS photometry in different passbands, they assigned probabilities to the dominant frequency of each star having a degree l of 0, 1, or 2. For 143 β Cep stars, they could identify a particular degree with a probability greater than 60%. However, the azimuthal orders of these dominant modes are not provided by the multi-passband identification method.

2.2. Stricter mode identification from rotational splitting

To determine the degree and azimuthal order of as many signals detected in each target's TESS light curve as possible, we searched for rotationally split multiplets. For the low-order modes of single, non-magnetic β Cep stars, these multiplets show up as series of up to $2l + 1$ roughly evenly spaced frequencies in the Fourier transform of a light curve.

Without prior information on a star's rotation and the identities of its pulsation modes, there are many possible combinations of detected modes that could plausibly form a multiplet. Hence, to avoid misidentifying multiplets, we constrained ourselves to candidates that satisfy a number of conditions based on the existing observations and the expected properties of β Cep pulsations. However, imposing a list of overly strict conditions can introduce selection biases and limit our sample size. Therefore, the identification of a potential multiplet was considered sufficiently secure when it satisfied at least four of these five conditions:

1. All $2l + 1$ frequencies in the multiplet are detected.
2. The rotational splitting in the candidate multiplet should be compatible with the $f_{\rm rot} \sin i$ estimate from *Gaia* if it is available. To that end, we defined the mean rotational splitting as $\overline{\Delta f} \equiv \langle \frac{f_m - f_0}{m} \rangle$, wherein f_m is the multiplet's frequency of azimuthal order m (so f_0 is the zonal mode frequency) and $\langle\rangle$ indicates a mean over the non-zonal ($m \neq 0$) modes. $\overline{\Delta f}$ should either be greater than the lower limit $f_{\rm rot} \sin i$, or no more than 2σ or a factor 2 smaller to account for the Ledoux constant (Ledoux 1951).
3. The identification of the candidate multiplet's degree must not contradict the multi-colour analysis of the dominant mode by Fritzewski et al. (2025). How this condition is applied depends on the dominant mode identity and to which multiplet the dominant mode belong.
   a) If the dominant mode is part of the candidate multiplet, the probability of the degree suggested by the rotational splitting must be at least 40% in Fritzewski et al. (2025).
   b) If the dominant mode belongs to a multiplet other than the candidate multiplet, we compared $\overline{\Delta f}$ of and the candidate multiplet. Since rotational splitting in either multiplet can be reduced by up to 50% due to the Ledoux constant, we demanded $\overline{\Delta f}$ in each multiplet to differ less than a factor 2. If there are no observed signals in this frequency window around a high-amplitude signal, we considered that signal as a radial mode.
   c) If Fritzewski et al. (2025) identified the dominant mode as a radial mode with a probability of at least 60%, this condition was neglected for candidate multiplets that do not include the dominant mode.
4. The broader a multiplet's rotational splitting, the more likely it becomes for an unrelated mode to be misidentified as part of the multiplet. Moreover, rotational splitting in rapidly rotating stars is expected to be more asymmetric, which complicates mode identification. Therefore, we selected multiplets with $\overline{\Delta f} < 0.75\,{\rm d}^{-1}$, following observations of confirmed multiplets of β Cep stars in the literature.
5. Rotationally split p-mode multiplets in slow to moderate rotators are nearly symmetric with a dimensionless asymmetry $|A_{|m|}| = \frac{2f_0 - f_m - f_{-m}}{f_m + f_{-m}}$ of the order of a few times 10^{-2} (Guo et al. 2024). Consequently, we sought multiplets with $|A_{|m|}| < 0.10$ to prevent the misidentification of unrelated signals that approximately line up by coincidence.

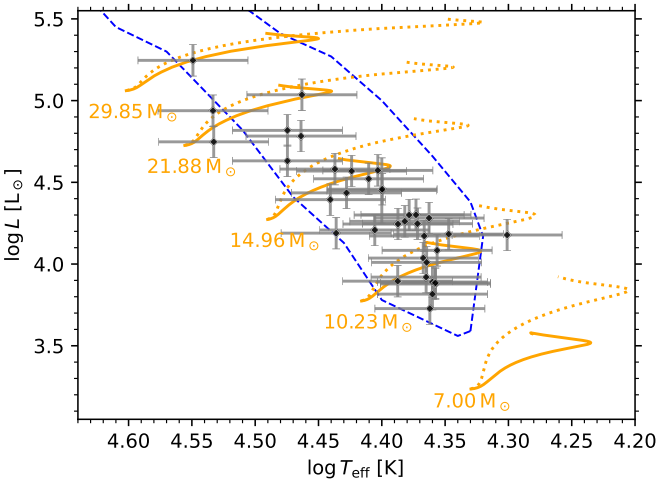

Fig. 1: Hertzsprung-Russell diagram with the targets in our sample. The dashed blue line indicates the p-mode instability strip of Burssens et al. (2020). Some examples of evolutionary tracks from our model grid are shown in orange. Solid lines indicate the models with the weakest core overshoot and envelope mixing and dotted lines those with the strongest mixing.

2.3. Literature pulsators

To validate the novel asteroseismic forward modelling strategy described in Sect. 4 and to expand our sample further, we added β Cep stars with forward modelling in the literature. Our study is focussed on pulsations of degree $l = 0, 1, 2$ since those are the only identifications provided by Fritzewski et al. (2025) and are the most commonly observed in space photometry of β Cep pulsators. Due to the requirements of our modelling approach, we selected literature stars with at least one identified rotationally split multiplet and either an identified radial mode or another multiplet.

Six well-known β Cep stars fulfil these conditions, namely HD 129929 (e.g., Aerts et al. 2003, 2004b; Dupret et al. 2004), ν Eri (e.g., Aerts et al. 2004a; Ausseloos et al. 2004; De Ridder et al. 2004; Pamyatnykh et al. 2004; Jerzykiewicz et al. 2005; Dziembowski & Pamyatnykh 2008; Suárez et al. 2009), β CMa (e.g., Handler et al. 2003; Desmet et al. 2006; Mazumdar et al. 2006; Shobbrook et al. 2006), θ Oph (e.g., Handler et al. 2005; Briquet et al. 2005, 2007; Lovekin & Goupil 2010), HD 192575 (Burssens et al. 2023; Vanlaer et al. 2025; Vandersnickt et al. 2025), and 12 Lac (e.g., Handler et al. 2006; Dziembowski & Pamyatnykh 2008; Desmet et al. 2009). Notably, 12 Lac was already included in the sample of Fritzewski et al. (2025), who agreed with the mode identification by Handler et al. (2006) and Desmet et al. (2009). For the other five validation stars, we adopted the observed $T_{\rm eff}$, L, frequencies, and identifications of l and, if available, m reported in the literature.

Our work presents the largest sample of β Cep stars with enough identified modes to perform asteroseismic forward modelling in a homogeneous way. Table D.1 summarises all observational input used for our modelling. Of the 36 stars we successfully model in Sect. 4, 24 have an identified radial mode and 17 have more than one identified rotationally split multiplet. Figure 1 shows our targets in the Hertzsprung-Russell diagram (HRD) alongside some evolutionary tracks.

Table 1: Parameter space of our MESA-StORM grid.

parameter	code	min.	max.	number
M [$M_\odot$]	MESA	7.00	29.85	43
$\log D_{\rm mix,0}$ [cm^2 s^{-1}]	MESA	1.0 ; 2.0	5.0 ; 6.0	5
$f_{\rm ov}$	MESA	0.005	0.035	7
$X_{\rm c}$	MESA	0.0001	0.701	118
$f_{\rm rot}/f_{\rm crit}$	StORM	0.0	0.40	41

3. Grid of stellar models

Asteroseismic forward modelling requires stellar models with predictions of their pulsation frequencies to match observations to. One can either use a model grid with medium resolution or an initial grid with poor resolution which is continually refined around a star's optimal parameter values. This second approach was commonly used by past studies on individual β Cep stars (e.g., Dupret et al. 2004; Briquet et al. 2007; Suárez et al. 2009; Burssens et al. 2023). Since we seek to model a large number of pulsators, refining the grid for each star is not feasible. Figure 1 shows our stars are spread over a broad area of the HRD, so we require a grid covering the entire β Cep instability strip.

3.1. Models of stellar structure and evolution

We computed a new grid of non-rotating stellar models using the stellar structure and evolution code Modules for Experiments in Stellar Astrophysics (MESA) version r24.08.1 (Paxton et al. 2011, 2013, 2015, 2018, 2019; Jermyn et al. 2023). These models were optimised for asteroseismic modelling by improving the spatial resolution around burning and convective regions using the scheme of Burssens et al. (2023). The models contain the solar metal fractional abundances from Asplund et al. (2009). We used the corresponding radiative opacity grids of the Opacity Project library (Seaton 2005), except at low temperatures where they are blended with the opacity tables of Ferguson et al. (2005). The equation of state is a blend of FreeEOS (Irwin 2004) and Skye (Jermyn et al. 2021). Our custom nuclear network contains 32 isotopes covering the four cold CNO-cycles and the α-backbone up to ^{56}Fe and ^{56}Ni. We exclusively used the nuclear rates of the JINA REACLIB (Cyburt et al. 2010).

We used the Ledoux criterion for convection and set the mixing-length parameter $\alpha_{\rm MLT} = 2.0$. Since most of our stars lack strong observational constraints on their metallicity from high-resolution spectroscopy, we fixed the initial metallicity Z at 0.014. The consequences of this choice are assessed in Sect. 4.1.5. We included the levels of core-boundary and envelope mixing as free parameters in the models. Core-boundary mixing was implemented as exponential overshooting, which begins a distance of $0.005\,H_P$ into the convective core, wherein H_P is the pressure scale height. The core overshoot parameter $f_{\rm ov}$ varies from 0.005 to 0.035 in steps of 0.005. Beyond the overshooting zone, the mixing profile represents envelope mixing caused by internal gravity waves. Based on the hydrodynamical simulations by Rogers & McElwaine (2017), the mixing profile is set to $D_{\rm mix} = D_{\rm mix,0}\frac{\rho_0}{\rho}$, with ρ the local density and ρ_0 the density at the base of the envelope. As shown by the simulations of Varghese et al. (2023) and confirmed by the observational calibration of Mombarg et al. (2025b), mixing by internal gravity waves increases with mass. Therefore, we let $D_{\rm mix,0}$ vary from 10 to 10^6 cm^2 s^{-1} in logarithmic steps $\Delta \log D_{\rm mix,0} = 1$ in the model grid. However, to prevent the models with $M < 13\,M_\odot$ from being completely mixed, we set the upper limit of $D_{\rm mix,0}$ to 10^5 cm^2 s^{-1} for that mass regime. On the other hand, $D_{\rm mix,0} = 10$ cm^2 s^{-1} is too low to meaningfully mix models more massive than $13\,M_\odot$, which is required to match asteroseismic observations (Moravveji et al. 2015). As such, the lower limit for $D_{\rm mix,0}$ is set to 10^2 cm^2 s^{-1} for these masses.

To sample the entire β Cep space, we computed main sequence models with 43 values for M between 7 and $30\,M_\odot$ in logarithmic steps of $\Delta \log M = 0.015$. This results in typical steps in M of $0.5\,M_\odot$ with tighter sampling around lower M. Each MESA run created output at 118 values of central hydrogen fraction $X_{\rm c}$ between 0.701 and 0.0001, with the resolution increasing as $X_{\rm c}$ decreases. This fine age resolution ensures there is a model reasonably close to the star's true parameters. Table 1 summarises the parameter space of our grid.

3.2. Oscillation computations

To predict the pulsation frequencies of $l = 0, 1, 2$ modes in our stellar models, we employed the adiabatic oscillation code Stellar Oscillations with Rotation (StORM, Vanlaer et al. submitted)[1], which is optimised for the low-order modes of β Cep stars. It includes the second-order rotation effects due to the Coriolis force and rotational deformation, approximated by the Chandrasekhar-Milne expansion to second-order (Chandrasekhar 1933; Tassoul 1978) applied to a spherical stellar input model. This deformation increases the star's total size and hence reduces all mode frequencies. The oscillation frequencies are further perturbed by coupling between spherical harmonics, including toroidal components (Saio 1981; Lee & Baraffe 1995). As frequencies of different azimuthal order are perturbed at different levels, these second-order effects of rotation result in asymmetric rotationally split multiplets.

Recently, Mombarg et al. (2025a) compared the pulsations of 2D stellar models to those computed with StORM from 1D models to evaluate StORM's ability to constrain an internal magnetic field from asymmetry rotational splitting. Their study considers rotation frequencies $f_{\rm rot}$ below 20% of the Keplerian critical rotation rate $f_{\rm crit}$. They showed that the rotational asymmetries predicted by StORM are in general accurate enough for asteroseismic modelling of β Cep stars with identified low-order modes. Thanks to StORM's predictions of the asymmetry of multiplets, we can include the observed rotational splitting of non-radial modes as additional constraints in the asteroseismic forward modelling, as also proposed by Suárez et al. (2010). This strongly constrains $f_{\rm rot}$ in particular, which we include as a fifth free parameter in our forward modelling (see Table 1).

We computed the oscillations at $f_{\rm rot}$ in the range 0-40% of the Keplerian critical rotation rate $f_{\rm crit}$ in steps of 1% of $f_{\rm crit}$. This pushes beyond the 20% limit below which Mombarg et al. (2025a) showed StORM to be fully reliable. As such, the modelling of some modes may only be approximate in the most

[1] https://storm.stellar-oscillations.org/

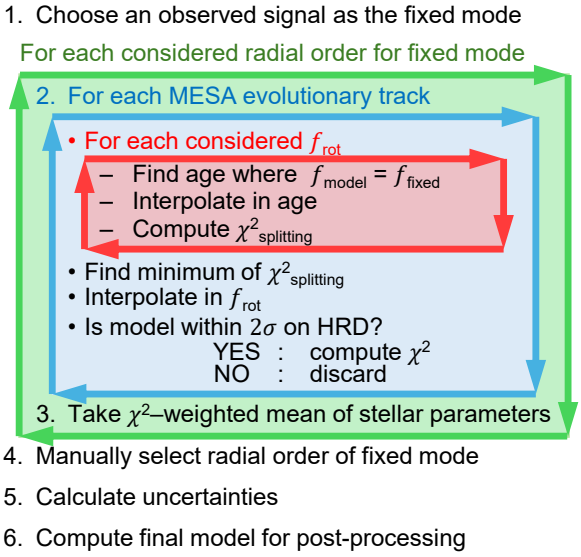

Fig. 2: Step-by-step overview of the forward modelling method applied to each star. The steps in coloured boxes are repeated for each considered radial order of the fixed mode (green), for each evolutionary track in our model grid (blue), and for each considered rotation rate (red). Each step is explained in its own section in the main text.

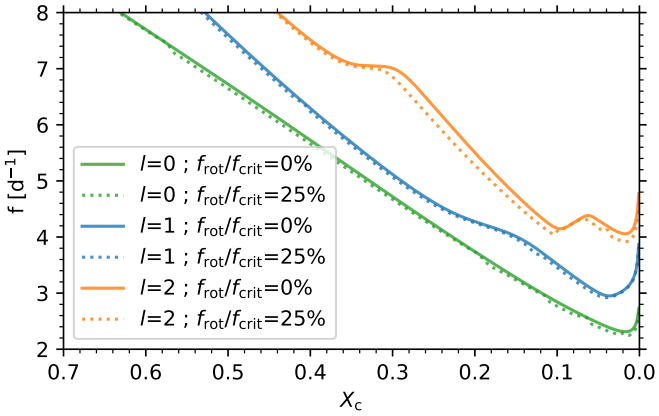

Fig. 3: Evolution of the radial (green), dipole (blue), and quadrupole (orange) zonal p_1-mode frequencies of a non-rotating (solid lines) and rotating (dashed lines) model.

rapidly rotating stars in our sample. Nevertheless, this is still superior to a first-order approximation resulting in symmetrical splittings. While most parameters in stars with $f_{rot} > 20\,\% f_{crit}$ are still well-constrained, some stars' $l = 1$ multiplets are rather poorly reproduced, as detailed in Sect. 5.

Although β Cep stars are known to feature differential rotation, our oscillation computations assume rigid-body rotation because the rotation profiles of the sample stars are not known a priori. This choice limits the dimensionality and makes our modelling problem solvable while still accounting for the effects of rotation in a more advanced way than past β Cep forward modelling applications. The framework outlined by Suárez et al. (2010) would permit to further constrain the rotation profiles, though this has not yet been applied to an observed β Cep pulsator. Such an additional step is beyond our global sample study. Instead, we placed constraints on the rotation profiles of our stars using these Uniformly rotating models in Section 7.

We scanned for frequencies of modes with degrees $l = 0, 1, 2$ between 2 and 15 d^{-1}, which reliably includes the radial orders n_{pg} from -3 to +5 that we consider in our modelling. `StORM` defines n_{pg} using the Eckart-Scuflaire-Osaki scheme (Eckart 1961; Scuflaire 1974; Osaki 1975), except for $l = 1$ modes for which it uses the Takata scheme (Takata 2006).

4. Asteroseismic forward modelling

In this section, we detail our modelling approach, demonstrate its reliability using the six validation stars in our sample, and present some essential modelling results. All observational input data used in the modelling are available in an electronic table, a snippet of which is shown in Table D.1.

4.1. Step-by-step modelling breakdown

Our forward modelling approach is inspired by that of Ausseloos et al. (2004), who first fitted the radial mode of ν Eri to find its age before fitting the remaining zonal modes. This two-step approach reduces the computational cost of the forward modelling, which is of great importance when modelling an entire sample of β Cep pulsators. We implemented a similar methodology, but generalised it in two important ways. First, we account for the second-order effect of rotation on the mode frequencies through STORM's model of stellar deformation. Consequently, the age found from a mode frequency depends on the rotation rate, so we determined the rotation rate in a consistent way during the forward modelling rather than in a 'a posteriori' analysis step. Secondly, not all targets in our sample have an identified radial mode. Therefore, the age of each stellar model in the grid may be determined from a different identified mode, which we refer to as the star's 'fixed mode'.

Our modelling methodology is shown schematically in Fig. 2. Each of these six steps is explained in a section below.

4.1.1. Selecting the fixed mode

We first select an identified signal as the fixed mode used to determine the optimal age. Following Ausseloos et al. (2004) and Desmet et al. (2006), we always use a radial mode as the fixed mode if one is identified in the observations. Figure 3 shows the evolution of three zonal mode frequencies at different rotation rates. The radial mode frequency decreases monotonically with age until the model approaches the TAMS. Meanwhile, the non-radial modes display some bumps due to mixed mode behaviour and avoided crossings (Burssens et al. 2023; Guo et al. 2024). Consequently, radial modes are preferred over non-radial modes as they always allow for a unique age determination from one observed frequency in each evolutionary track.

For targets without an identified radial mode, we selected a zonal mode as the fixed mode since they are less dependent on f_{rot} than non-zonal modes. The bumps seen in Fig. 3 are more common for modes of lower radial order and thus lower frequency. Therefore, we picked the identified zonal mode with the highest frequency as the fixed mode. This has the disadvantage that these modes are more affected by the second-order rotation effect stellar deformation (e.g., Saio 1981), although the rotation optimisation procedure described in Sect. 4.1.2 accounts for that effect.

Should the zonal non-radial mode in a star still be influenced by these bumps, the age established from the fixed mode would

vary chaotically with the other free parameters. This behaviour showed up in the modelling of one target, which was subsequently excluded from our sample as the age could not be reliably determined.

4.1.2. Fixing age and rotation frequency for each evolutionary track

With a chosen fixed mode at hand and assuming its radial order is known (we revisit this assumption in Sect. 4.1.4), we compared the observed and predicted frequencies in an evolutionary track of MESA-StORM models. We created a cubic interpolation spline of the predicted fixed mode frequency for the different ages. Next, we found the age when the prediction spline matches the observed fixed mode frequency. Then similar cubic interpolation splines were created for all predicted frequencies and stellar parameters to produce an asteroseismic model at the fixed age. The errors incurred by this interpolation are smaller than the observational uncertainties.

Because of StORM's inclusion of the second-order rotational effect caused by the stellar deformation, zonal mode frequencies depend on the rotation rate. Therefore, we repeated the above age fixing for each considered rotation rate to find the relation between the fixed age and rotation rate. To select an optimal rotation frequency and thus age, we computed for each of these models at different rotation rates the merit function $\chi^2_{\text{splitting}} = \sum_j \frac{(\Delta f_{j,\text{obs}} - \Delta f_{j,\text{model}})^2}{\sigma^2_{\Delta f_j}}$, with Δf the rotational frequency splitting and $\sigma_{\Delta f}$ its uncertainty. The index j iterates over all identified non-zonal modes. $\chi^2_{\text{splitting}}$ represents how well a model's frequency predictions ('model') reproduce the observed rotational splitting ('obs'). Using a cubic interpolation spline for $\chi^2_{\text{splitting}}$ against $f_{\text{rot}}/f_{\text{crit}}$, we minimise $\chi^2_{\text{splitting}}$ to find the best-fit value for $f_{\text{rot}}/f_{\text{crit}}$ in this evolutionary track. Finally, the predicted frequencies and stellar parameters in the age-fixed models are interpolated in $f_{\text{rot}}/f_{\text{crit}}$.

By establishing the optimal age and rotation rate from a fixed mode and the measured rotational splittings, we reduced an entire evolutionary track of thousands of MESA-StORM models down to one. This procedure was performed for each evolutionary track –characterised by M, $\log D_{\text{mix},0}$, and f_{ov}– in our model grid. To ensure these models were compatible with the spectroscopic constraints provided by *Gaia* DR3, we discarded the selected models outside the observed 2σ error ellipse in the HRD.

4.1.3. Statistical parameter estimation

As a measure for the quality of each selected model within the 2σ error ellipse in the HRD, we computed $\chi^2 = \sum_i \frac{(Q_{i,\text{obs}} - Q_{i,\text{model}})^2}{\sigma^2_{Q_i}}$. For the fitted quantities Q_i, we used the identified zonal mode frequencies $f_{j,0}$, identified rotational splitting Δf_j, $\log T_{\text{eff}}$, and $\log L$.[2] The contributions of $\log T_{\text{eff}}$ and $\log L$ to χ^2 are small due to their large observational uncertainties. As the radial orders of the observed modes are not known a priori, we scanned all radial orders n_{pg} and used the one with a zonal frequency closest to the observed zonal frequency of the multiplet. We considered the range of radial orders $n_{\text{pg}} = (-3, \ldots, 5)$. In the end, none of the observed signals were matched with the extrema -3 and 5, which shows that our range in n_{pg} was sufficiently broad.

[2] Note that the frequencies $f_{m,j}$ of non-zonal non-radial modes are not directly fitted.

We computed statistical parameter estimates from a weighted average over the remaining models in the 2σ error ellipse in the HRD with weights given by $\exp(-\frac{\chi^2}{2})$. This reduces the dependence on the grid resolution by allowing the free parameters to take on values between the grid output. Moreover, the weighted standard deviation provides an estimate of the statistical uncertainty $\sigma_{Q,\text{stat}}$ for each quantity Q.

4.1.4. Identifying the radial orders

In the modelling steps described above, it was assumed that the radial order of the fixed mode was known. However, this is not the case. Therefore, we repeated steps 1 to 3, each time assuming a different radial order for the fixed mode. Then, we assessed the modelling outcomes from the different analyses and manually selected the most likely radial order based on three hierarchical conditions:

1. We always favoured a radial order that produced a model with frequencies that explained unidentified signals in the observations.
2. If the first condition did not result in a favoured radial order, we examined the smallest χ^2 values of each modelling run and used these as a measure of the overall fit quality. We preferred a certain n_{pg} if the minimal χ^2 is at most half of the minimal χ^2 obtained with different n_{pg}.
3. If the previous conditions did not provide a best n_{pg}, we selected the model closest to the observed position in the HRD.

For radial fixed modes, we tested $n_{\text{pg}} = 1, 2, 3$. Higher order radial modes were not considered as these have never been observed in any β Cep star and are predicted to be stable (Pamyatnykh 1999; Rehm et al. 2024). For non-radial fixed modes, we also tried $n_{\text{pg}} = -1, -2, -3$ on top of $n_{\text{pg}} = 1, 2, 3$ as β Cep stars are known to feature non-radial p- and g-modes. No star in our sample favoured $n_{\text{pg}} = -3$ for its fixed mode, so we did not try any higher-order g-modes. Finally, if the fixed mode has degree $l = 2$, we also considered that the fixed mode may be an f-mode, represented by $n_{\text{pg}} = 0$.

4.1.5. Errors and systematic uncertainties

Several sources of uncertainty for each estimated parameter Q can be considered. The statistical spread between the selected models is represented by the weighted standard deviation $\sigma_{Q,\text{stat}}$ computed in step 3. These neglect the theoretical uncertainties on predicted pulsation frequencies due to the choice of frozen input physics, which may be orders of magnitude larger than the typical observed frequency error. Therefore, we set the uncertainty on our identified frequencies to 10^{-3} d^{-1}, which is the typical theoretical uncertainties for β Cep stars (Aerts et al. 2018).

Even taking into account the uncertainty caused by the choice of input physics, almost all stars have unrealistically small $\sigma_{Q,\text{stat}}$ from step 3. This occurs when the frequency differences between models of different (M, $\log D_{\text{mix},0}$, f_{ov}) are much larger than the frequency uncertainty, which leads one model to dominate the statistical estimate of Q. This is a known phenomenon from grid modelling and makes it difficult to obtain statistical values for (M, $\log D_{\text{mix},0}$, f_{ov}) between the grid output. In these cases we adopt an uncertainty on the free parameters of at least half a grid step. We thus set an uncertainty on Q of $\sigma_Q = \max(\sigma_{Q,\text{stat}}, \frac{\Delta Q_{\text{grid}}}{2})$, with ΔQ_{grid} the grid step for $Q = M, \log D_{\text{mix},0}, f_{\text{ov}}$. These increased uncertainties are then propagated to all other stellar parameters through the theoretical

correlations between those parameters and M, $\log D_{\rm mix,0}$ in the closest grid output.

Another source of systematic uncertainty is our fixed $Z = 0.014$, as β Cep pulsators display a range of metallicities (e.g., Niemczura & Daszyńska-Daszkiewicz 2005, and references in Table 2). A weighted standard deviation of the metallicity in the 31 β Cep field stars reported by Niemczura & Daszyńska-Daszkiewicz (2005) shows the spread on Z is approximately 0.003. The unknown metallicity affects the modelled stellar mass (e.g., Ausseloos et al. 2004; Dupret et al. 2004; Aerts et al. 2018). To estimate this additional uncertainty on M, we computed additional `MESA-StORM` models at $Z = 0.011$ and $Z = 0.017$. From these models, we calculated the change in a pulsation frequency f_j of a particular mode j due to a change in metallicity $\Delta Z = 0.003$. Then we assessed the change in mass ΔM_j required to compensate for these frequency changes as $\Delta M_j = \left(\frac{{\rm d}f_j}{{\rm d}M}\right)^{-1} \frac{{\rm d}f_j}{{\rm d}Z}\Delta Z$. This mass shift depends approximately linearly on M, only weakly on $X_{\rm c}$, and strongly on the mode identification j. Subsequently, we calculated the typical relative mass shift $\mathcal{M}_j = \frac{\Delta M}{M}$ of each mode j. As a conservative estimate for the uncertainty due to unknown metallicity $\sigma_{M,Z}$, we used $\sigma_{M,Z} = \max_j(\mathcal{M}_j)M$ with j going over the known mode identifications in each target. As our final estimate of the error on M, we took $\max(\sigma_{M,\rm stat}, \frac{\Delta M_{\rm grid}}{2}, \sigma_{M,Z})$. $\sigma_{M,Z}$ proved to be the largest mass uncertainty in all but one of our stars. Again, this increased uncertainty was propagated to the other parameters.

For $f_{\rm rot}$, we consider one more source of uncertainty. As detailed in Sect. 5, the rotational splitting is not adequately reproduced by `StORM` in some rapidly rotating stars, which may lead to $f_{\rm rot}$ getting under- or overestimated. To quantify this effect, we computed $\overline{\Delta f}$ from the observations and our `StORM` model. An additional error on $f_{\rm rot}$ is then computed as $\Delta f_{\rm rot} = f_{\rm rot}\left(1 - \frac{\overline{\Delta f}_{\rm model}}{\overline{\Delta f}_{\rm obs}}\right)$. If $|\Delta f_{\rm rot}| > \sigma_{f_{\rm rot}}$, it is used as a unidirectional error on $f_{\rm rot}$ depending on its sign.[3]

4.1.6. Compute model at statistical parameter values

After establishing the fixed mode's radial order, we are left with a set of statistical estimates for the five free parameters (M, $\log D_{\rm mix,0}$, $f_{\rm ov}$, $X_{\rm c}$, $f_{\rm rot}$) computed in step 3. However, no model output is available in the grid at precisely these statistical values. Subsequently, we computed a new `MESA-StORM` model for each star to ensure consistency in the further analyses of these models in Sects. 5 and 7.

4.2. Validation of the procedure

We tested our modelling methodology on the six validation stars described in Sect. 2.3. Figure 4 compares the observed frequencies and our models. Overall, we successfully match the observed zonal frequencies except for the $l = 2$ mode in 12 Lac, which is strongly coupled to its radial mode. This makes it difficult to model that $l = 2$ mode, hence why it was excluded from the observational input by Desmet et al. (2009). The rotational splittings are reproduced very well except for some multiplets in HD 192575 and 12 Lac, the two most rapidly rotating stars of the six validation stars. We also find the same $n_{\rm pg}$ as reported in the six studies summarised in Table 2. This shows that the conditions used for the radial order identification summarised in Sect. 4.1.4 are sound.

We compare five essential stellar parameters from our modelling with the values reported in the literature in Table 2. The uncertainties or value ranges on these five parameters are included where available in the literature. Our values mostly agree with the literature within 1σ, which verifies the quality of our sample modelling. In some stars, there is a discrepancy in M due to our fixing of $Z = 0.014$ while the literature models vary Z. These mass differences also propagate to discrepancies in $\log g$ and $X_{\rm c}$, which is especially the case in β CMa. Overall good agreement is obtained and differences are understood in terms of different input physics.

4.3. Summary of modelling results

We applied our modelling procedure to 38 targets selected from the sample of Fritzewski et al. (2025). We found a satisfactory model for 31 of these targets. Together with the five literature stars this produces a final sample of 36 modelled β Cep pulsators. The modelling results of the 36 β Cep pulsators are summarised in Table D.2.

A corner plot of the five free parameters is given in Fig. A.1. Our sample covers most of the parameter space quite well, though only two stars have $M > 20\,M_\odot$. The maximum value of $X_{\rm c}$ is 0.43 so our sample only probes the second half of the main sequence, in line with the β Cep instability strips presented by Pamyatnykh (1999) and Burssens et al. (2020). A similar range in $X_{\rm c}$ was reported by Fritzewski et al. (2025), who modelled the $T_{\rm eff}$, L and one zonal mode frequency in 119 β Cep stars based only on the identified l of the dominant mode. The modelling outcomes of the stars in both modelled samples are compared in Appendix B.1. While there is an overall agreement in M, our modelling greatly improved the estimates of $X_{\rm c}$.

Our inability to find a good model for seven stars could indicate that their mode identifications were incorrect since the identified degrees from Fritzewski et al. (2025) are not absolute. Moreover, rotational splitting can be misidentified by the chance alignment of different modes. Alternatively, the pulsation frequencies in these stars may be affected by some physical processes not accounted for in our model grid, such as binary interactions (e.g., Sun et al. 2023) or magnetic fields (e.g., Mathis & Bugnet 2023; Das et al. 2024; Guo et al. 2024).

5. Importance of second-order rotational effects

Thanks to the size of our sample, we can now examine the systematic impact of second-order rotational effects in forward modelling of β Cep pulsator. Most past measurements of $f_{\rm rot}$ from rotational splitting $\Delta f = f_m - f_0$ in β Cep stars relied on first-order Ledoux splitting $\Delta f = m(1 - C_{nl})f_{\rm rot}$, where the Ledoux constant C_{nl} (Ledoux 1951) was computed for the best forward model based on using only the identified zonal frequencies (e.g., Aerts et al. 2003; Dupret et al. 2004; Pamyatnykh et al. 2004; Desmet et al. 2009; Burssens et al. 2023). Even studies that included second-order rotation effects (e.g., Briquet et al. 2007; Dziembowski & Pamyatnykh 2008; Suárez et al. 2009; Vanlaer et al. 2025) estimated $f_{\rm rot}$ a posteriori. In our modelling, the rotationally induced asymmetric splitting and zonal frequency shifts played a key role cf. Sect. 4.1.2).

To evaluate how the second-order rotation effects included in `StORM` affect the measured $f_{\rm rot}$, we computed C_{nl} using the oscillation code `GYRE` version `7.2.1` (Townsend & Teitler 2013).

[3] As the other stellar parameters are not directly dependent on the rotation rate, this unidirectional systematic error is not propagated.

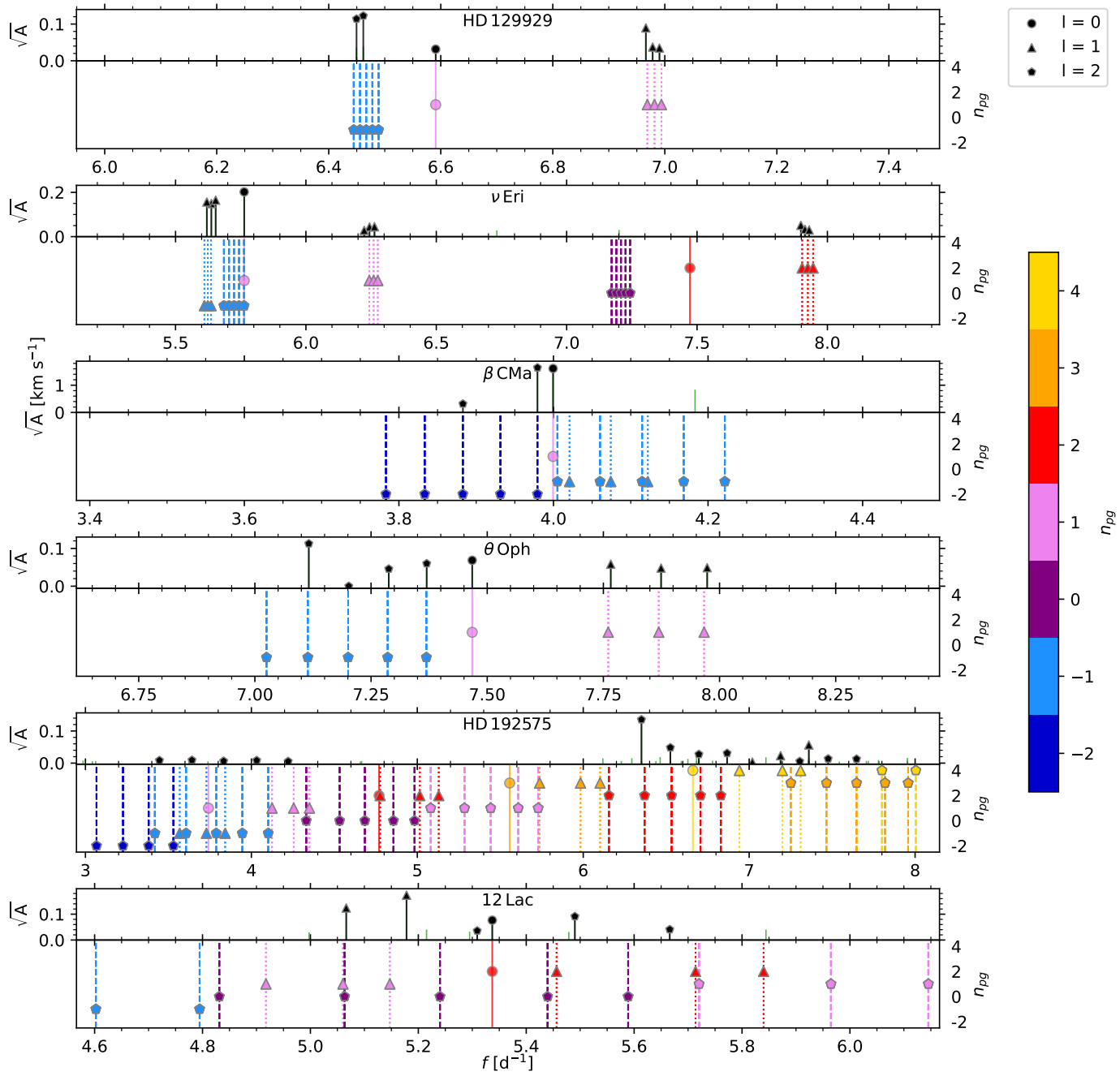

Fig. 4: Comparing the observed (top) and best model's frequencies (bottom) for the six validation stars. The x-axis is different for each star. The y-axis in the top panel shows the square root of the relative flux amplitude (except in β CMa, whose spectroscopically detected signals are given in km s^{-1}). Unidentified signals are green lines while identified ones are black and are topped by a marker indicating the degree. In the bottom panel, the colours and y-axis indicate the radial order. Markers have a thin grey outline to distinguish overlapping markers.

Emulating previous studies, we estimated $f_{\rm rot}$ for each rotationally split multiplet as $f_{\rm rot} = \overline{\Delta f}/(1 - C_{nl})$. Figure 5 compares these estimates to our consistently optimised $f_{\rm rot}$ from `StORM`. The two estimates start to deviate when $f_{\rm rot} > 10\% f_{\rm crit}$. We thus conclude that second-order rotational effects should not be ignored in β Cep modelling for stars rotating faster than approximately $10\% f_{\rm crit}$.

Figure 5 shows that the optimal $f_{\rm rot}$ found with `StORM` tends to be smaller than $f_{\rm rot}$ estimated from `GYRE`. The difference in $f_{\rm rot}$ is especially prominent for $l = 1$ multiplets at high $f_{\rm rot}$. This occurs because `StORM` often predicts large asymmetric splittings for dipole modes, such that $|\Delta f|$ is greater for retrograde modes ($m < 0$) than for prograde modes ($m > 0$). Indeed, the top panel of Fig. 6 shows that the predicted asymmetry tends to be larger than observed for $l = 1$ modes. This is partly because we looked for multiplets with a small asymmetry, as described in Sect. 2. Consequently, our forward modelling method reproduces the splitting of the retrograde modes reasonably well, yet sometimes underestimates the prograde mode splitting. As a result, the mean rotational splitting $\overline{\Delta f}$ can get underestimated by our

Table 2: Comparison of the parameter estimates from our forward modelling to modelling results reported in the literature.

	Our statistical model					Model(s) in literature						
star	M [$M_\odot$]	$\log T_{\rm eff}$ [K]	$\log g$ [cm s^{-2}]	$X_{\rm c}$	$f_{\rm rot}$ [d^{-1}]	M [$M_\odot$]	$\log T_{\rm eff}$ [K]	$\log g$ [cm s^{-2}]	$X_{\rm c}$	$f_{\rm rot}$ [d^{-1}]	Z	Ref.
HD 129929	8.9(6)	4.34(2)	3.892(16)	0.318(19)	0.0132^{+1}_{-44}	9.35	4.350	3.905	0.353	0.0127-0.0147	0.0188	(1)
ν Eri	8.6(6)	4.32(2)	3.803(17)	0.267(17)	0.0265^{+4}_{-4}	7.83	4.306	3.789	...	...	0.0155	(2)
β CMa	12.0(7)	4.370(16)	3.644(12)	0.17(2)	0.060^{+14}_{-4}	13.5(5)	4.373	3.529	0.128(3)	0.054(9)	0.021	(3)
θ Oph	8.0(5)	4.33(2)	3.948(17)	0.393(17)	0.107^{+3}_{-11}	8.2(3)	4.348(5)	3.950(6)	0.38(2)	0.1068-0.1075	0.012	(4)
HD 192575	13.0(9)	4.39(3)	3.62(5)	0.23(3)	0.188^{+7}_{-7}	$13.0^{+0.3}_{-1.3}$	4.401^{+28}_{-5}	3.66^{+10}_{-5}	0.24^{+1}_{-12}	...	0.014	(5)
12 Lac	11.4(8)	4.361(18)	3.662(14)	0.167(6)	0.156^{+9}_{-28}	10.0-14.4	4.343-4.408	3.64-3.70	...	0.186-0.190	0.010-0.015	(6)

Notes. The initial metallicity in our models is not shown as it is fixed to 0.014. 12 Lac is shown separately due to its limited capacity to test our forward modelling. We compare our model of θ Oph to that of Briquet et al. (2007) rather than the more recent study by Lovekin & Goupil (2010) because the latter kept the initial mass fixed. Our results for ν Eri are compared to Ausseloos et al. (2004)'s model instead of Suárez et al. (2009) who used an initial hydrogen mass fraction of $X = 0.50$ which is too different from ours to merit comparison. For consistency, the model results shown here used only the eight frequencies modelled in Ausseloos et al. (2004), though the results of ν Eri below included all ten detected by Jerzykiewicz et al. (2005) and modelled by Suárez et al. (2009). Similarly, we included 12 Lac's $(n, l) = (0, 2)$ multiplet in our modelling, which Desmet et al. (2009) reported but did not fit. Herein we added a new frequency detected in the TESS light curve. The literature results of HD 192575 are from Vanlaer et al. (2025) Set 1, which matches our identifications of the radial orders.

References. (1) Dupret et al. (2004); (2) Ausseloos et al. (2004); (3) Mazumdar et al. (2006); (4) Briquet et al. (2007); (5) Vanlaer et al. (2025); (6) Desmet et al. (2009).

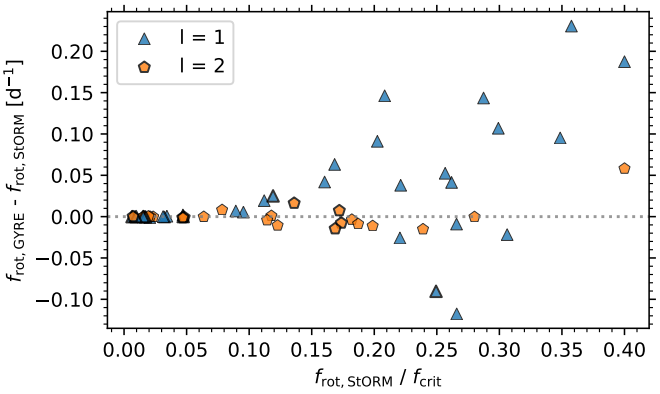

Fig. 5: Difference in rotation frequency from each identified multiplet by our self-consistent modelling using `StORM` and by the a posteriori step with `GYRE` against the relative rotation rate. Multiplets belonging to a validation stars are outlined in black. The grey dotted line shows where the two estimates agree.

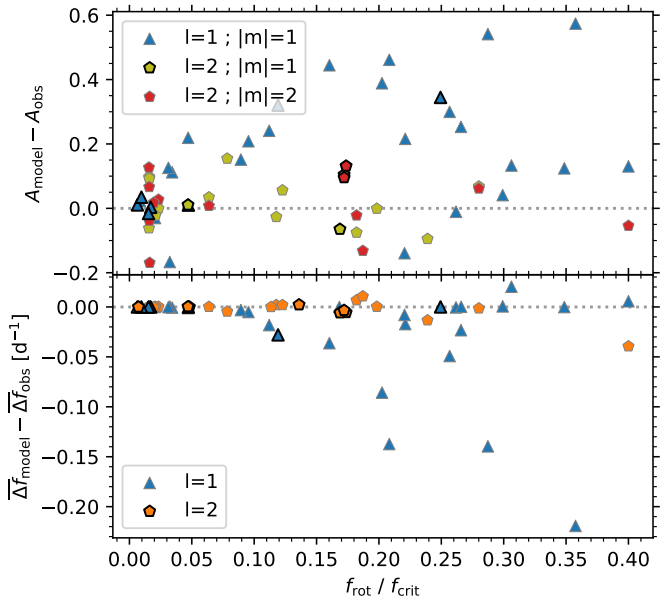

Fig. 6: Difference in asymmetry (top) and mean rotational splitting (bottom) from each multiplet between the model and observations against the relative rotation rate. Multiplets belonging to a validation star are outlined in black. The grey dotted line shows where the model reproduces the observation.

modelling, as demonstrated in Fig. 6's bottom panel. This may imply that we somewhat underestimate $f_{\rm rot}$ for some stars with identified prograde $l = 1$ modes rotating faster than $10\% f_{\rm crit}$. Our additional error on $f_{\rm rot}$ was introduced in Sect. 4.1.5 to compensate for this. All rotational splitting data used to compute that error and shown in these two figures are gathered in Table D.3.

The asteroseismic modelling methodology presented in Sect. 4.1 is the first applied to β Cep pulsators from a consistent fit to the rotational splitting using a second-order treatment of rotation. To examine the impact of these features, we repeated our forward modelling with two alternative methods. First, we re-analysed all stars with $f_{\rm rot}$ optimised for only a first-order rotation treatment using `GYRE` during step 2 of the modelling. Secondly, we removed the contribution of Δf_j to the χ^2 cost function in step 3. The methods and results from these two tests are only summarised here but elaborated on in Appendix B.2. Electronic tables summarising the results using these alternative methods are available at the CDS. The observed zonal frequencies are better reproduced when including the stellar deformation. In this respect, the incorporation of second-order effects improves the forward modelling quality. Moreover, our modelling with `StORM` improves the fit to the observed asymmetries and mean splittings for all $f_{\rm rot}$. On the other hand, the inclusion of Δf_j in the χ^2 cost function worsens the match with the observed zonal frequencies when $f_{\rm rot} > 20\% f_{\rm crit}$. Therefore, whether or not one should add

Δf_j in χ^2 depends on what stellar parameters one prioritises. As this study is primarily concerned with the rotational properties of β Cep stars, we included the rotational splittings in the cost function. Finally, the differences in all stellar parameters, except $f_{\rm rot}$, produced by these different modelling approaches are generally small. As such, the additional systematic uncertainties are modest, which justifies the exploitation of the results presented in the next Section.

In conclusion for this Section, a first-order treatment of the rotation cannot explain multiplet asymmetries. In that sense, our sample modelling treating the rotational deformation of the stars brings an essential improvement. Nevertheless, further future improvements can be considered. Aside from the limitations in `StORM`'s treatment of the rotational deformation, the star's actual rotation profile also affects multiplet asymmetries (Suárez et al. 2006, 2009, 2010). Given that we assumed rigid rotation in our oscillation computations, future derivations of the rotation profiles will allow for an upgrade in the quality of the modelling from the observed asymmetries. Moreover, some or all of these β Cep stars could possess strong internal magnetic fields (Vandersnickt et al. 2025), which counteract the rotationally induced asymmetric splitting (Mathis & Bugnet 2023; Das et al. 2024; Guo et al. 2024).

6. Behaviour of core mass and rotation rate

We now look for trends in the stellar structure parameters of the modelled β Cep stars. In particular, we examine the mass of the convective core given its importance to the star's later evolution and its chemical yields (e.g. Hirschi et al. 2005; Pedersen 2022; Brinkman et al. 2025). We also focus on the internal rotation to facilitate future angular momentum transport studies for a sample of high-mass stars, instead of only a handful as done so far.

6.1. Convective core mass

The convective cores of massive stars shrink as they evolve along the main sequence due to the changing opacity as hydrogen is fused into helium. This has already been studied from asteroseismology of γ Dor (e.g. Mombarg et al. 2021) and SPB stars (e.g. Pedersen 2022). With the forward modelling results of our β Cep sample, we can now asteroseismically calibrate the behaviour of the relative convective core mass $M_{\rm cc}/M$ across a higher mass range. To that end, we fitted $M_{\rm cc}/M$ against M and $X_{\rm c}$, as shown in Fig. 7. The best fitting relations are given by

$$M_{\rm cc}/M = -3.4(1.8)\,10^{-4}\left(\frac{M}{\rm M_\odot}\right)^2 + 0.0241(63)\,\frac{M}{\rm M_\odot} + 0.039(50)$$

$$M_{\rm cc}/M = 0.469(87)\,X_{\rm c} + 0.136(24)$$

$$M_{\rm cc}/M = -3.90(91)\,10^{-4}\left(\frac{M}{\rm M_\odot}\right)^2 + 0.0236(32)\,\frac{M}{\rm M_\odot} + 0.328(34)\,X_{\rm c} - 0.064(26)$$

The coefficients of determination of these three relations are 0.73, 0.45, and 0.93, respectively, which indicates that the bivariate fit explains most of the variability in $M_{\rm cc}/M$. Our results are in agreement with Johnston (2021), who compared $M_{\rm cc}$ from asteroseismology and eclipsing binaries to conclude that stars with a convective core possess a wide range of core masses.

The third panel of Fig. 7 suggests that $M_{\rm cc}/M$ increases with $f_{\rm ov}$ as overshooting provides the core access to more hydrogen from the envelope, although this relation is just barely not statistically significant. The final panel shows a correlation between $M_{\rm cc}/M$ and $f_{\rm rot}$, which is due to the $f_{\rm rot} - X_{\rm c}$ correlation seen in Fig. A.1. This relation between $f_{\rm rot}$ and $X_{\rm c}$ reflects the decrease of the internal rotation rate along the main sequence. Such a decrease is in line with the large sample of intermediate-mass main sequence stars in Aerts (2021); Aerts et al. (2025). Another significant correlation included in Fig. A.1 is between $f_{\rm ov}$ and $X_{\rm c}$, which indicates that core overshooting weakens as the stars evolve. Parametrised core overshooting is merely a reflection of core boundary mixing due to a multitude of instabilities occurring in this transition layer. Many of these instabilities are caused by the local rotation rate (see Heger et al. 2000; Aerts et al. 2019, for extensive discussions of these instabilities), meaning these last two correlations are likely connected.

6.2. Specific angular momentum of β Cep stars

The evolution of the specific angular momentum $J/M = 4\pi/3\, f_{\rm rot} R^2$ of a population of stars is used to study initial stellar rotation rates and angular momentum losses. Kraft (1967) discussed a decrease of $f_{\rm rot}$ with age in solar-type stars, indicating efficient angular momentum loss due to magnetic winds. The relation between J/M and stellar mass M, in particular the 'Kraft break' around 1.3 $\rm M_\odot$, has also been used to examine how the efficiency of angular momentum loss depends on stellar structure (Kawaler 1987, 1988). Aerts (2025) studied asteroseismic J/M values for approximately 3000 pulsating main-sequence stars with masses $M \in [1.3, 9]\,\rm M_\odot$. From the near-core rotation rate and assuming quasi-rigid rotation, they found another break in the $J/M(M)$ relation around $2.5 \pm 0.2\,\rm M_\odot$.

Using our sample of β Cep stars in the $M \in [8, 30]\,\rm M_\odot$ range, we test the upper limit of J/M in a higher mass regime. Figure 8 displays the $J/M(M)$ and $J/M(X_{\rm c})$ relations along with the high-mass upper limit in $J/M(M)$ presented by Aerts (2025). Our massive β Cep stars obey this upper limit, in agreement with the findings by Aerts (2025). For β Cep pulsators, the assumption of quasi-rigid rotation may be inaccurate just as found by Aerts (2025) for the B-stars. Nonetheless, the $J/M(M)$ upper limit remains over 50% above the $J/M(M)$ of our stars, which is comparable to the typical level of differential rotation in β Cep stars (Burssens et al. 2023, cf. Sect. 7).

There is no sign of J/M increasing as $X_{\rm c}$ decreases in the right panel of Fig. 8. In contrast, Aerts (2025) finds that J/M increases as $X_{\rm c}$ decreases for the more massive stars in their sample of intermediate-mass stars. That increase either means that some of these stars gained angular momentum from binary interactions or developed differential rotation. The lack of such a relation in our sample may indicate that the internal rotation profiles of our high-mass β Cep stars are different from those of the intermediate-mass stars of Aerts (2025). We investigate this in the next Section.

7. Differential rotation constraints in 17 β Cep stars

We now seek to constrain the rotation profiles in a subsample of our β Cep stars. Following Fritzewski et al. (2025), we placed an upper bound on the envelope-to-surface rotation ratio from our optimised internal rotation frequencies $f_{\rm rot,interior}$[4] and the projected surface velocities $f_{\rm rot,surface} \sin i$ estimated from *Gaia* spectroscopy. Figure 9 shows the relation between these two rotation measurements for 29 stars with an available estimate of

[4] The internal rotation rate was previously symbolised by $f_{\rm rot}$, but we add the 'interior' subscript here to distinguish it from the surface rotation rate.

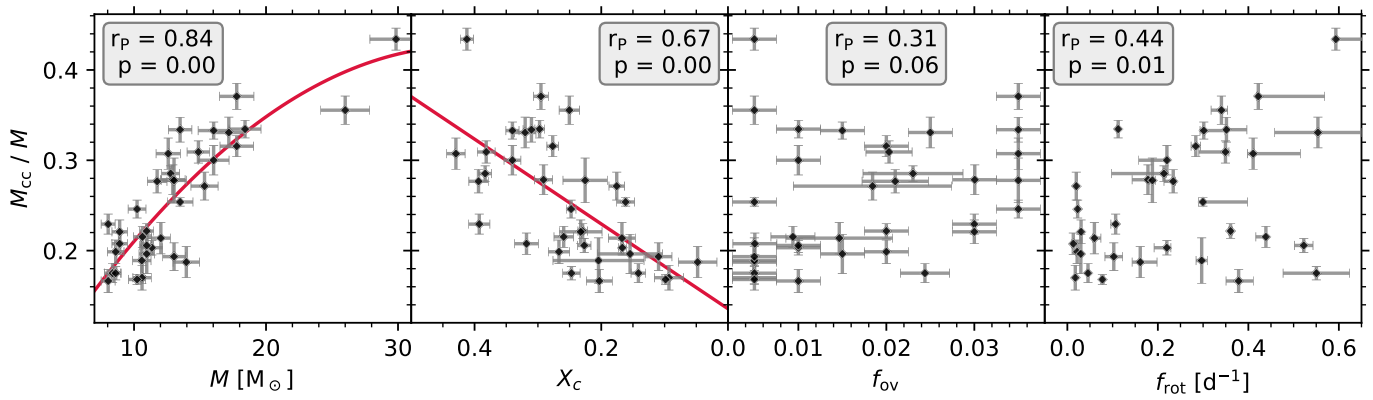

Fig. 7: Convective core mass relative to total stellar mass against the total mass (M), central hydrogen mass fraction (X_c), overshoot parameter (f_{ov}), and rotation frequency (f_{rot}). Red lines show a quadratic and linear fit against total mass and central hydrogen mass fraction, respectively. Boxes display the Pearson correlation coefficients and the p-values of the associated t-tests.

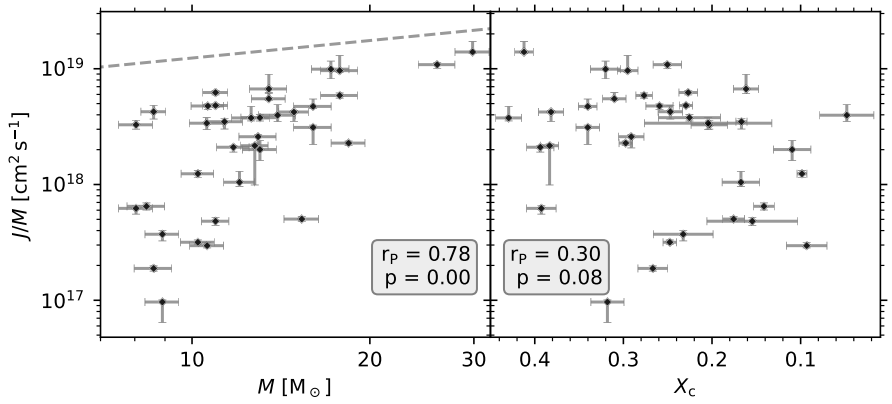

Fig. 8. Specific angular momentum of each star against its mass (left) and core hydrogen mass fraction (right). On the left panel, the grey dashed line indicates the upper limit on the specific angular momentum for stars more massive than 2.5 $M_\odot$ derived by Aerts (2025). Boxes show the Pearson correlation coefficients and the p-values of the associated t-tests.

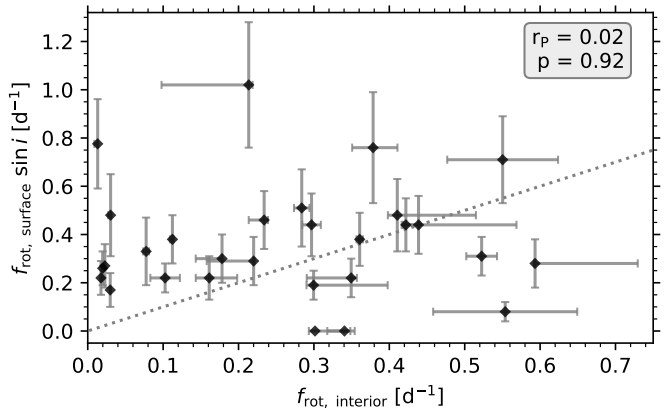

Fig. 9: Projected surface rotation frequency from *Gaia*'s ESP-HS pipeline against the interior rotation frequency when modelling all identified multiplets. The grey dotted line marks where the two measurements are equal. The Pearson correlation coefficient and the p-value of the associated t-test is included in a box. Two stars were assigned a surface rotation velocity of zero, which indicates that rotational broadening was not detected.

$f_{\rm rot,surface} \sin i$. Notably, they are uncorrelated, which is in part because $f_{\rm rot,surface} \sin i$ is only a lower limit of $f_{\rm rot,surface}$. On the other hand, broadening of spectroscopic lines by the pulsations can lead to $f_{\rm rot,surface} \sin i$ getting overestimated for our high-amplitude β Cep pulsators. Therefore, we turn to purely asteroseismic constraints on the internal rotation profile, which are more precise and unaffected by unknown projection factors.

In order to constrain the internal differential rotation of stars using rigidly rotating models, we re-analysed the 17 stars with more than one rotationally split multiplet. We re-model them once per multiplet. Each time, we included all identified zonal mode frequencies in the observational input, but only one multiplet's rotational splitting Δf_j. Consequently, $f_{\rm rot}$ is optimised for only that multiplet in modelling step 2. For consistency, the statistical parameter estimation of $f_{\rm rot}$ in step 3 still used the $\exp(-\chi^2/2)$ weights found when modelling all multiplets' Δf_j. Next, we computed the multiplet's rotational sensitivity kernel K_{nl}. All information on the $f_{\rm rot}$ estimates from each multiplet and their sensitivity kernels required to reproduce the results presented in this section are collected in Table D.4. Figure C.1 shows some examples of such sensitivity kernels, which are discussed further in Appendix C. The left panel of Fig. 10 shows the statistical $f_{\rm rot}$ for each multiplet against the normalised radius where it is most sensitive. The right panel plots the rotation rate normalised to that of the mode that is most sensitive closest to the surface. Normalised rotation rates below 1 indicate the rotation rate is greater at higher radius and vice versa.

The $f_{\rm rot}$ measurements vary by more than 10% in 14 of the 17 β Cep stars , showing that strong radial differential rotation is common among this subsample. Even the three stars with a small difference in $f_{\rm rot}$, such as θ Oph (shown in red in Fig. 10), might still be differential rotators. Figure C.1 shows that θ Oph's two

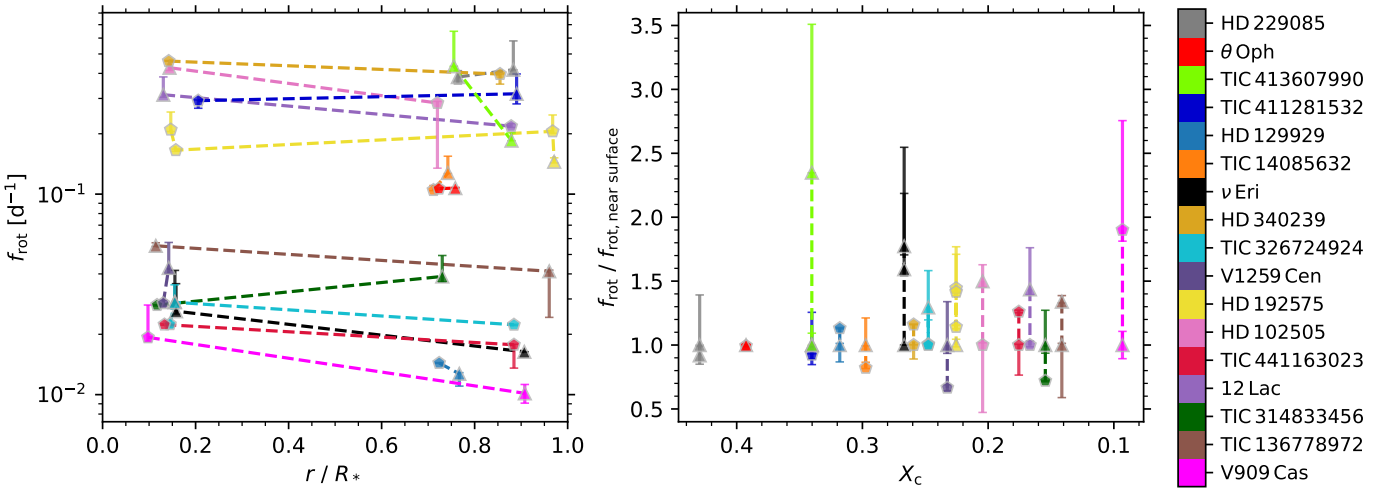

Fig. 10: Interior differential rotation in 17 stars with several rotationally split multiplets. The left panel shows the rotation frequency from a rotationally split multiplet at the radius where that multiplet is most sensitive. Rotation frequencies extracted from $l = 1$ and $l = 2$ multiplets are marked as triangles and pentagons, respectively. The right panel shows these rotation rates normalised by the rotation rate nearest the surface against the core hydrogen mass fraction. Each star has a unique colour indicated in the colourbar, which is sorted by central hydrogen mass fraction.

multiplets probe the same layers of the envelope, so it could still feature differential rotation in unprobed regions. The outward rotation gradient $\frac{\partial f_{\rm rot}}{\partial r}$ is most commonly negative, as observed before (Burssens et al. 2023). Nevertheless, there are four stars for which $f_{\rm rot}$ grows with r by over 10%. Such a strong outward increase in $f_{\rm rot}$ has not been detected in β Cep pulsators before. Only in the aforementioned θ Oph has an outward rotation increase of about 5% been suggested before (Briquet et al. 2007).

That strong differential rotation is so commonly detected in our sample is somewhat surprising as there are three biases against it. First, the low-order modes in β Cep stars are usually sensitive to broad regions of the stellar envelope, as shown in Fig. C.1. When the sensitivity kernels of two multiplets overlap, the difference in their optimal $f_{\rm rot}$ is diminished as they both average $f_{\rm rot}$ over the same layers. Secondly, there is a selection bias in our mode identification from rotational splitting. As discussed in Sect. 2.2, candidate multiplets with rotational splitting differing by more than a factor 2 were not included in our sample. Finally, our modelling is set up to reproduce all observed rotational splittings based on models assuming rigid rotation. Consequently, the difference in $f_{\rm rot}$ required to optimally reproduce the splitting of each multiplet individually is reduced. That we detect rotation differences greater than 10% in 14 out of 17 stars despite these biases strengthens the conclusion that strong radial differential rotation is common in β Cep stars.

Remarkably, three of the five stars with two multiplets probing $r/R_* > 0.5$ display an outwardly increasing rotation frequency, namely HD 229085 (grey), θ Oph (red), and TIC 14085632 (orange)). These stars could have undergone accretion during binary interactions as expected in this mass regime. Eight out of ten stars with one multiplet probing near the core and another one assessing the upper envelope have a negative rotation gradient. Combined, these trends may indicate that the typical rotation profile of β Cep pulsators is non-monotonic, featuring a relatively rapidly rotating core and a slower envelope with $\frac{\partial f_{\rm rot}}{\partial r} > 0$. The two of the three stars with three or more rotationally split multiplets, HD 192575 (yellow) and TIC 326724924 (cyan), also produce both positive and negative $\frac{\partial f_{\rm rot}}{\partial r}$. The rotation inversions of HD 192575 by Vanlaer et al. (2025) showed that it has a core-to-envelope rotation ratio no greater than two and its rotation profile is not monotonic. Furthermore, both 2D hydrodynamical simulations (e.g., Rogers & Ratnasingam 2025) and 1D stellar structure models including transport by waves (e.g., Neiner et al. 2020) can produce such non-monotonic rotation profile in high-mass main sequence stars. As a conclusion, there is mounting evidence that non-monotonic differential rotation occurs in β Cep stars.

To help identify and calibrate the underlying angular momentum transport mechanisms, the rotation gradient should be observed at various points throughout the envelope and at different stages along the main sequence in yet more β Cep stars. Here we are limited by β Cep stars only occurring in the second half of the main sequence (cf. Sect. 4.3). On top of that, the mode excitation of β Cep pulsations is also not uniform throughout their evolution. As seen in the right panel of Fig. 10, all five stars that probe at different points in the upper envelope have $X_{\rm c} > 0.29$. This makes them among the least evolved stars of this subsample of 17 stars. Ten out of eleven stars that probe both the near-core region and outer envelope are all more evolved with $X_{\rm c} < 0.28$. The computations of mode excitation by Rehm et al. (2024) in a 9 $M_\odot$ stellar model indicate that several p-modes, which probe the envelope, are only excited while the star is young. Once the star is more evolved, it excites more and higher-order g-modes, which are most sensitive to the near-core layers. Consequently, it may be difficult to observe the envelope rotation gradient in evolved stars and the core-to-envelope rotation ratio in relatively young β Cep pulsators. Nonetheless, their value to constraining angular momentum transport makes seeking such detections a worthwhile effort. Moreover, that the relatively young TIC 411281532 probes both the near-core layers and envelope demonstrates it is possible to find β Cep stars providing these constraints.

In conclusion, measurable differential rotation is common in β Cep stars. The level of differentiality we could measure in our sample goes up to approximately a factor 2.5. This implies that the uncertainty on J/M in Fig. 8 due to the radial differential rotation is small enough that our stars still obey the upper limit

in Aerts (2025). Moreover, as differential rotation in β Cep stars appears to be non-monotonic and β Cep pulsations probe a variety of different layers, the presented J/M may be overestimated. Therefore, the conclusions from Sect. 6.2 regarding the specific angular momentum remain valid.

8. Summary and conclusions

We presented a sample of 36 asteroseismically modelled β Cep stars with the aim to exploit their potential to constrain angular momentum transport on the main sequence. This marks the first population of β Cep stars with forward asteroseismic modelling. For most stars in this sample, Fritzewski et al. (2025) provided identifications of the modes' degrees, which we complemented with identifications of degrees and azimuthal orders from rotational splitting. For our forward modelling, we created a new grid of `MESA` main sequence models with a wide range in mass, age, core overshoot, and envelope mixing. The oscillations in these models were computed using the state-of-the-art `StORM` code, which includes second-order rotation effects. Using these improved oscillation predictions, we developed a novel forward modelling approach for β Cep pulsators that consistently takes rotation into account.

Making use of the size of our sample, we calibrated the evolution of the convective core mass and its mass-dependency. We found that the core overshoot weakens with age, reflecting the shrinking core of these massive main sequence stars. Consequently, stellar models should ideally implement some time-dependent core overshooting scheme. Like in intermediate-mass main sequence stars, the rotation rate decreases as the stars evolve. Moreover, our β Cep stars obey the specific angular momentum relations of intermediate-mass stars.

One notable shortcoming of our modelling is our overestimation of the asymmetry of rotationally split dipole multiplets, which indicates some important physics is missing or oversimplified in our modelling. Internal magnetic fields are an obvious candidate as they are known to reduce the asymmetry of rotationally split multiplets. However, unambiguously disentangling the effects of both magnetism and rotation from asymmetries alone is difficult. This issue is alleviated if a multiplet displays both rotational and magnetic splitting, resulting in more than $2l+1$ components. HD 192575 is currently the only known β Cep star with such splitting (Vandersnickt et al. 2025). Consequently, a population level study including magnetic effects is not plausible until more β Cep pulsators with magnetic splitting are discovered.

An observational avenue to continue improving our understanding of β Cep stars is to further expand the sample to fill out the broad parameter space. In particular, there is still a shortage of β Cep stars more massive than $20\,M_\odot$. Further, more targets with enough rotationally split multiplets to measure the internal rotation rate near the core and throughout the envelope at different ages would also be highly beneficial. The upcoming PLATO space telescope (Rauer et al. 2025) is capable of providing the necessary photometry to detect the pulsation frequencies of several dozen β Cep pulsators with high precision (Nascimbeni et al. 2025). Meanwhile, both ground- and space-based multi-colour observations of β Cep stars have proven their capability to identify those pulsation signals. As shown by our work, these mode identifications can then be further refined from rotational splitting.

We successfully constrained radial differential rotation in 17 stars, increasing the sample of β Cep stars with purely asteroseismic measurements of differential rotation more than threefold. An overall trend emerged suggesting that the inner region near the convective core rotates faster than the envelope. For the few stars offering the information, we find that the rotation rate often increases outwardly in the envelope. Such a rotation gradient is expected for stars that experienced accretion in their recent past and/or are subject to the action of internal gravity waves. Combined with rotation inversions and rotation profiles in multi-dimensional hydrodynamical simulations, we conclude that non-monotonic differential rotation is common in β Cep stars. Testing which angular momentum transport mechanisms can explain these rotation profiles will require stellar modelling using new generations of stellar structure and evolution models with realistic transport mechanisms in order to verify if they reproduce all the observed rotational splitting.

Data availability

The complete versions of Tables D.1, D.2, D.3, and D.4 are only available in electronic form at `https://github.com/Mathijs-Vanrespaille/Vanrespaille_BetaCepheiForwardModelling.git` (placeholder, to be replaced with CDS information). The `Python` code used to perform our forward modelling is publicly available at `https://github.com/Mathijs-Vanrespaille/BCep_forward_modelling.git`. The `MESA` stellar models, including the `StORM` oscillation computations, can be freely accessed at the KU Leuven Research Data Repository (link to be added). Meanwhile, the `MESA` work directory and `StORM` setup can be found at the following Zenodo repository (link to be added). Electronic figures similar to Figs. 4 and C.1 for all 36 β Cep stars with a good model in our sample are available at the Zenodo repository (link to be added).

Acknowledgements. The authors thank the anonymous referee for their feedback. MV warmly thanks Hannah Brinkman for her advice in adapting our `MESA` inlists and for designing the nuclear network and acknowledges Ehsan Moravveji for his assistance in setting up the `MESA` grid computations. He also thanks Noi Shitrit, Tami Rogers, Miriam Rodriguez-Sanchez, Jelle Vandersnickt, Zhao Guo, and Pablo Huijse for useful conversations. Helpful comments on the manuscript were provided by Alex Kemp, Joey Mombarg, Michel Rieutord, Laura Scott, and Keegan Thomson-Paressant. The `MESA` and `StORM` computations were done at the Flemish Supercomputer Centre (VSC). MV has received funding from the KU Leuven Research Council (doctoral mandate grant DB/24/008). VV gratefully acknowledges support from the Research Foundation Flanders (FWO) under grant agreement N° 1156923N (PhD Fellowship). DJF and CA acknowledge support from the Flemish Government under the long-term structural Methusalem funding program by means of the project SOUL: Stellar evolution in full glory, grant METH/24/012 at KU Leuven. MV and CA acknowledge financial support from the European Research Council (ERC) under the Horizon Europe programme (Synergy Grant agreement N° 101071505: 4D-STAR). While partially funded by the European Union, views and opinions expressed are however those of the authors only and do not necessarily reflect those of the European Union or the European Research Council. Neither the European Union nor the granting authority can be held responsible for them. CA also acknowledges the Belgian Federal Science Policy Office (BELSPO) for the provision of financial support in the framework of the PRODEX Programme of the European Space Agency (ESA).

Software: This research made use of the `astropy` (Astropy Collaboration et al. 2022), `h5py` (Collette 2013), `matplotlib` (Hunter 2007), `NumPy` (Harris et al. 2020), `pandas` (Wes McKinney 2010), and `SciPy` (Virtanen et al. 2020) `Python` packages. We used the `MESA` (Paxton et al. 2011, 2013, 2015, 2018, 2019; Jermyn et al. 2023) stellar structure and evolution code to compute our new grid of stellar models and the codes `StORM` (Vanlaer et al. submitted) and `GYRE` (Townsend & Teitler 2013) to perform the oscillation computations.

References

Aerts, C. 2021, Reviews of Modern Physics, 93, 015001
Aerts, C. 2025, arXiv e-prints, arXiv:2511.02909
Aerts, C., Christensen-Dalsgaard, J., & Kurtz, D. W. 2010, Asteroseismology (Springer Netherlands)

Aerts, C. & De Cat, P. 2003, Space Sci. Rev., 105, 453
Aerts, C., De Cat, P., Handler, G., et al. 2004a, MNRAS, 347, 463
Aerts, C., Mathis, S., & Rogers, T. M. 2019, ARA&A, 57, 35
Aerts, C., Molenberghs, G., Michielsen, M., et al. 2018, ApJS, 237, 15
Aerts, C., Thoul, A., Daszyńska, J., et al. 2003, Science, 300, 1926
Aerts, C. & Tkachenko, A. 2024, A&A, 692, R1
Aerts, C., Van Reeth, T., Mombarg, J. S. G., & Hey, D. 2025, A&A, 695, A214
Aerts, C., Waelkens, C., Daszyńska-Daszkiewicz, J., et al. 2004b, A&A, 415, 241
Amard, L., Palacios, A., Charbonnel, C., et al. 2019, A&A, 631, A77
Asplund, M., Grevesse, N., Sauval, A. J., & Scott, P. 2009, ARA&A, 47, 481
Astropy Collaboration, Price-Whelan, A. M., Lim, P. L., et al. 2022, ApJ, 935, 167
Augustson, K. C. & Mathis, S. 2019, ApJ, 874, 83
Ausseloos, M., Scuflaire, R., Thoul, A., & Aerts, C. 2004, MNRAS, 355, 352
Auvergne, M., Bodin, P., Boisnard, L., et al. 2009, A&A, 506, 411
Bessila, L., Deckx van Ruys, A., Buriasco, V., et al. 2025, A&A, 700, A25
Borucki, W. J., Koch, D., Basri, G., et al. 2010, Science, 327, 977
Bowman, D. M. 2020, Frontiers in Astronomy and Space Sciences, 7, 70
Brinkman, H. E., Tkachenko, A., & Aerts, C. 2025, A&A, 702, A119
Briquet, M., Lefever, K., Uytterhoeven, K., & Aerts, C. 2005, MNRAS, 362, 619
Briquet, M., Morel, T., Thoul, A., et al. 2007, MNRAS, 381, 1482
Briquet, M., Neiner, C., Aerts, C., et al. 2012, MNRAS, 427, 483
Burssens, S., Bowman, D. M., Aerts, C., et al. 2019, MNRAS, 489, 1304
Burssens, S., Bowman, D. M., Michielsen, M., et al. 2023, Nature Astronomy, 7, 913
Burssens, S., Simón-Díaz, S., Bowman, D. M., et al. 2020, A&A, 639, A81
Chandrasekhar, S. 1933, MNRAS, 93, 390
Collette, A. 2013, Python and HDF5 (O'Reilly Media)
Cyburt, R. H., Amthor, A. M., Ferguson, R., et al. 2010, ApJS, 189, 240
Das, S. B., Einramhof, L., & Bugnet, L. 2024, A&A, 690, A217
De Ridder, J., Telting, J. H., Balona, L. A., et al. 2004, MNRAS, 351, 324
Decressin, T., Mathis, S., Palacios, A., et al. 2009, A&A, 495, 271
Degroote, P., Briquet, M., Catala, C., et al. 2009, A&A, 506, 111
Deheuvels, S., Doğan, G., Goupil, M. J., et al. 2014, A&A, 564, A27
Desmet, M., Briquet, M., Mazumdar, A., & Aerts, C. 2006, Communications in Asteroseismology, 147, 113
Desmet, M., Briquet, M., Thoul, A., et al. 2009, MNRAS, 396, 1460
Di Mauro, M. P., Ventura, R., Cardini, D., et al. 2016, ApJ, 817, 65
Dupret, M. A., Thoul, A., Scuflaire, R., et al. 2004, A&A, 415, 251
Dziembowski, W. A. & Pamyatnykh, A. A. 2008, MNRAS, 385, 2061
Eckart, C. 1961, Physics of Fluids, 4, 791
Eze, C. I. & Handler, G. 2024, ApJS, 272, 25
Ferguson, J. W., Alexander, D. R., Allard, F., et al. 2005, ApJ, 623, 585
Fouesneau, M., Frémat, Y., Andrae, R., et al. 2023, A&A, 674, A28
Fritzewski, D. J., Vanrespaille, M., Aerts, C., et al. 2025, A&A, 698, A253
Gaia Collaboration, Prusti, T., de Bruijne, J. H. J., et al. 2016, A&A, 595, A1
Gaia Collaboration, Vallenari, A., Brown, A. G. A., et al. 2023, A&A, 674, A1
García, R. A. & Ballot, J. 2019, Living Reviews in Solar Physics, 16, 4
Guo, Z., Bedding, T. R., Pamyatnykh, A. A., et al. 2024, MNRAS, 535, 2927
Handler, G., Jerzykiewicz, M., Rodríguez, E., et al. 2006, MNRAS, 365, 327
Handler, G., Shobbrook, R. R., Jerzykiewicz, M., et al. 2004, MNRAS, 347, 454
Handler, G., Shobbrook, R. R., & Mokgwetsi, T. 2005, MNRAS, 362, 612
Handler, G., Shobbrook, R. R., Uytterhoeven, K., et al. 2012, MNRAS, 424, 2380
Handler, G., Shobbrook, R. R., Vuthela, F. F., et al. 2003, MNRAS, 341, 1005
Harris, C. R., Millman, K. J., van der Walt, S. J., et al. 2020, Nature, 585, 357
Heger, A., Langer, N., & Woosley, S. E. 2000, ApJ, 528, 368
Hekker, S. & Christensen-Dalsgaard, J. 2017, A&A Rev., 25, 1
Hey, D. & Aerts, C. 2024, A&A, 688, A93
Heynderickx, D., Waelkens, C., & Smeyers, P. 1994, A&AS, 105, 447
Hirschi, R., Meynet, G., & Maeder, A. 2005, A&A, 443, 581
Hunter, J. D. 2007, Computing in Science & Engineering, 9, 90
Irwin, A. W. 2004, The FreeEOS Code for Calculating the Equation of State for Stellar Interiors I: An Improved EFF-Style Approximation for the Fermi-Dirac Integrals, https://freeeos.sourceforge.net/
Jermyn, A. S., Bauer, E. B., Schwab, J., et al. 2023, ApJS, 265, 15
Jermyn, A. S., Schwab, J., Bauer, E., Timmes, F. X., & Potekhin, A. Y. 2021, ApJ, 913, 72
Jerzykiewicz, M., Handler, G., Shobbrook, R. R., et al. 2005, MNRAS, 360, 619
Johnston, C. 2021, A&A, 655, A29
Kawaler, S. D. 1987, PASP, 99, 1322
Kawaler, S. D. 1988, ApJ, 333, 236
Kraft, R. P. 1967, ApJ, 150, 551
Kurtz, D. W. 2022, ARA&A, 60, 31
Kurtz, D. W., Saio, H., Takata, M., et al. 2014, MNRAS, 444, 102
Labadie-Bartz, J., Handler, G., Pepper, J., et al. 2020, AJ, 160, 32
Ledoux, P. 1951, ApJ, 114, 373
Lee, U. & Baraffe, I. 1995, A&A, 301, 419
Li, G., Aerts, C., Bedding, T. R., et al. 2024, A&A, 686, A142
Li, G., Van Reeth, T., Bedding, T. R., et al. 2020, MNRAS, 491, 3586
Lovekin, C. C. & Goupil, M.-J. 2010, A&A, 515, A58
Maeder, A. 2009, Physics, Formation and Evolution of Rotating Stars
Mathis, S. & Bugnet, L. 2023, A&A, 676, L9
Mathis, S., Decressin, T., Eggenberger, P., & Charbonnel, C. 2013, A&A, 558, A11
Mathis, S. & Zahn, J. P. 2004, A&A, 425, 229
Mathis, S. & Zahn, J. P. 2005, A&A, 440, 653
Mazumdar, A., Briquet, M., Desmet, M., & Aerts, C. 2006, A&A, 459, 589
Mombarg, J. S. G., Van Reeth, T., & Aerts, C. 2021, A&A, 650, A58
Mombarg, J. S. G., Vanlaer, V., Das, S. B., et al. 2025a, arXiv e-prints, arXiv:2511.09617
Mombarg, J. S. G., Varghese, A., & Ratnasingam, R. P. 2025b, A&A, 695, A255
Moravveji, E., Aerts, C., Pápics, P. I., Triana, S. A., & Vandoren, B. 2015, A&A, 580, A27
Nascimbeni, V., Piotto, G., Cabrera, J., et al. 2025, A&A, 694, A313
Neiner, C., Lee, U., Mathis, S., et al. 2020, A&A, 644, A9
Niemczura, E. & Daszyńska-Daszkiewicz, J. 2005, A&A, 433, 659
Osaki, Y. 1975, PASJ, 27, 237
Ouazzani, R.-M., Marques, J. P., Goupil, M.-J., et al. 2019, A&A, 626, A121
Pamyatnykh, A. A. 1999, Acta Astron., 49, 119
Pamyatnykh, A. A., Handler, G., & Dziembowski, W. A. 2004, MNRAS, 350, 1022
Paxton, B., Bildsten, L., Dotter, A., et al. 2011, ApJS, 192, 3
Paxton, B., Cantiello, M., Arras, P., et al. 2013, ApJS, 208, 4
Paxton, B., Marchant, P., Schwab, J., et al. 2015, ApJS, 220, 15
Paxton, B., Schwab, J., Bauer, E. B., et al. 2018, ApJS, 234, 34
Paxton, B., Smolec, R., Schwab, J., et al. 2019, ApJS, 243, 10
Pedersen, M. G. 2022, ApJ, 930, 94
Pedersen, M. G., Aerts, C., Pápics, P. I., et al. 2021, Nature Astronomy, 5, 715
Pedersen, M. G., Escorza, A., Pápics, P. I., & Aerts, C. 2020, MNRAS, 495, 2738
Pereira, A. W., Janot-Pacheco, E., Emilio, M., et al. 2024, A&A, 686, A20
Rauer, H., Aerts, C., Cabrera, J., et al. 2025, Experimental Astronomy, 59, 26
Rehm, R., Mombarg, J. S. G., Aerts, C., et al. 2024, A&A, 687, A175
Ricker, G. R., Winn, J. N., Vanderspek, R., et al. 2015, Journal of Astronomical Telescopes, Instruments, and Systems, 1, 014003
Rogers, T. M., Lin, D. N. C., McElwaine, J. N., & Lau, H. H. B. 2013, ApJ, 772, 21
Rogers, T. M. & McElwaine, J. N. 2017, ApJ, 848, L1
Rogers, T. M. & Ratnasingam, R. P. 2025, ApJ, 983, L38
Saio, H. 1981, ApJ, 244, 299
Scuflaire, R. 1974, A&A, 36, 107
Seaton, M. J. 2005, MNRAS, 362, L1
Shi, X.-d., Qian, S.-b., Zhu, L.-y., et al. 2024, ApJS, 271, 28
Shitrit, N. & Arcavi, I. 2024, AJ, 167, 65
Shobbrook, R. R., Handler, G., Lorenz, D., & Mogorosi, D. 2006, MNRAS, 369, 171
Suárez, J. C., Andrade, L., Goupil, M. J., & Janot-Pacheco, E. 2010, Astronomische Nachrichten, 331, 1073
Suárez, J. C., Goupil, M. J., & Morel, P. 2006, A&A, 449, 673
Suárez, J. C., Moya, A., Amado, P. J., et al. 2009, ApJ, 690, 1401
Sun, M., Townsend, R. H. D., & Guo, Z. 2023, ApJ, 945, 43
Takata, M. 2006, PASJ, 58, 893
Talon, S., Zahn, J. P., Maeder, A., & Meynet, G. 1997, A&A, 322, 209
Tassoul, J.-L. 1978, Theory of rotating stars (Princeton University Press)
Tayler, R. J. 1973, MNRAS, 165, 39
Townsend, R. H. D. & Teitler, S. A. 2013, MNRAS, 435, 3406
Triana, S. A., Corsaro, E., De Ridder, J., et al. 2017, A&A, 602, A62
Triana, S. A., Moravveji, E., Pápics, P. I., et al. 2015, ApJ, 810, 16
Vandersnickt, J., Vanlaer, V., Vanrespaille, M., & Aerts, C. 2025, A&A, 704, L13
Vanlaer, V., Bowman, D. M., Burssens, S., et al. 2025, A&A, 701, A5
Vanlaer, V., Mombarg, J., Guo, Z., & Townsend, R. submitted, A&A
Varghese, A., Ratnasingam, R. P., Vanon, R., Edelmann, P. V. F., & Rogers, T. M. 2023, ApJ, 942, 53
Virtanen, P., Gommers, R., Oliphant, T. E., et al. 2020, Nature Methods, 17, 261
Wes McKinney. 2010, in Proceedings of the 9th Python in Science Conference, ed. Stéfan van der Walt & Jarrod Millman, 56 – 61
Zahn, J.-P. 1992, A&A, 265, 115

Appendix A: Parameter space and correlations

Figure A.1 shows a corner plot of the five free parameters in our modelling. These distributions and some of the correlations were already discussed in Sects. 4.3 and 6.1, respectively. Here we examine some of the remaining correlations or lack thereof.

The Pearson correlation coefficients with the initial mass M reported in Fig. A.1 are dominated by the two most massive stars. If these two targets are neglected, the correlations with $f_{\rm rot}$ and $X_{\rm c}$ become greatly weakened and are no longer significant. However, a significant positive correlation between M and $\log D_{\rm mix,0}$ aappears when neglecting the two most massive stars. This new correlation reflects how the mixing coefficients must be greater in more massive stars to mix the greater mass over a longer radius. The slope of $\log D_{\rm mix,0}$ against M is similar to that found in the simulations of Varghese et al. (2023) for the middle main sequence. This justifies our decision to increase $\log D_{\rm mix,0}$ for the models with $M > 13.03\,{\rm M}_\odot$ (see Sect. 3.1), although how we constructed the $\log D_{\rm mix,0}$ parameter grid is also partly responsible for the relation with M.

Besides the correlation between $f_{\rm ov}$ and $X_{\rm c}$ discussed in Sect. 6.1, there is no significant correlations including either of the mixing parameters $f_{\rm ov}$ or $\log D_{\rm mix,0}$. Notably, $f_{\rm ov}$ is not significantly negatively correlated with $f_{\rm rot}$, despite theoretical work suggesting that rotation can reduce the efficiency of convection and core-boundary mixing (e.g., Tayler 1973; Augustson & Mathis 2019; Bessila et al. 2025).

There are several causes behind this lack of clear relations. First, not all β Cep pulsations are sensitive to the envelope (e.g., the top right panel of Fig. C.1), which makes it difficult to constrain $\log D_{\rm mix,0}$ in some β Cep stars. Secondly, the β Cep pulsation class is inherently diverse due to the wide range in mass, age, metallicity, and rotation rate, which complicates the relations between these parameters. Thirdly, the broad parameter space is not covered uniformly or completely by our sample, which features a gap in the mass range between approximately 20 and 25 $\rm M_\odot$ in the mass histogram of Fig. A.1. Finally, differential rotation is common in β Cep stars, while the optimised $f_{\rm rot}$ probe diverse regions of the stars. Therefore, $f_{\rm rot}$ may not be representative of the star as a whole, which potentially clouds relations between $f_{\rm rot}$ and other free parameters.

Appendix B: Different modelling approaches

Appendix B.1: Comparison to Fritzewski et al. (2025)

Here we seek to test how the addition of more identified frequencies and our more intricate modelling approach improves upon the modelling of Fritzewski et al. (2025). For the 24 stars in both samples, we compare three essential parameters in Fig. B.1. Overall, there is a clear agreement in the stellar mass M, except at the highest and lowest masses. This is because Fritzewski et al. (2025) used the stellar model grid of Burssens et al. (2023) which only covers $M \in [9, 21.5]\,M_\odot$, while we found that these stars' masses range from $8\,{\rm M}_\odot$ to $30\,{\rm M}_\odot$. The differences in the central hydrogen mass fraction $X_{\rm c}$ are large, demonstrating that this work significantly improved the estimates of $X_{\rm c}$ and therefore the age. This superior $X_{\rm c}$ constraint also results in an improved estimate for the convective core mass due to the strong relation with $X_{\rm c}$ discussed in Sect. 6.1.

Appendix B.2: Further evaluating the impact of second-order rotation effects

As shown in Sect. 5, `StORM` tends to overestimate the asymmetry of the rotational splitting in $l = 1$ multiplets of β Cep stars with a rotation frequency $f_{\rm rot}$ greater than 10% of the Keplerian critical rotation frequency $f_{\rm crit}$. This subsequently leads to the estimated $f_{\rm rot}$ being smaller compared to an extraction of $f_{\rm rot}$ from a simplified, 'a posteriori' estimate based on the first-order rotation treatment of the `GYRE` oscillation code. When $f_{\rm rot} = 0$, `StORM` reproduces the frequencies computed with `GYRE` to within observational errors (Vanlaer et al. submitted). Consequently, we can evaluate the impact of the second-order rotation effects in our forward modelling by comparing the modelling results from these two codes. The most notable second-order effects are the asymmetric rotational splitting and stellar deformation reducing mode frequencies.

Here we compare the modelling outcomes of different modelling methodologies in order to answer the following questions:

- Does the reduction of mode frequencies due to stellar deformation and shifts in zonal frequency from mode coupling lead to a better match with the observed zonal frequencies?
- Does our consistent inclusion of asymmetric rotational splitting Δf_j in the χ^2 merit function in modelling step 3 worsen the fit of the other observations?
- How does the choice of oscillation code and modelling strategy affect our estimates of the stellar parameters?

We repeated the modelling of our 36 stars using the same grid of stellar models, though with the oscillation computations performed with `GYRE`. The modelling method was identical to the one described in Sect. 4.1 with two notable changes. First, zonal mode frequencies f_0 are unchanged by rotation to first order. Therefore, the procedure of fixing the age of each evolutionary track using the fixed mode described in Sect. 4.1.2 only needed to be performed for $f_{\rm rot} = 0$. Subsequently, the process of interpolating between various at different ages also became unnecessary. Secondly, the optimal $f_{\rm rot}$ is determined from the observed rotational splitting $\Delta f_{{\rm obs},j}$ by calculating the Ledoux constant $C_{{\rm nl},j}$ (Ledoux 1951) with `GYRE` and minimising $\sum_{\rm j}(\Delta f_{{\rm obs},j} - m_{\rm j}(1 - C_{{\rm nl},j})f_{\rm rot})^2/\sigma^2_{\Delta f_{{\rm obs},j}}$. With this new procedure, the optimal $X_{\rm c}$ and $f_{\rm rot}$ were once again determined for each evolutionary track and only models within 2σ on the observed position in the HRD were retained. Afterwards, modelling steps 3 to 6 were followed as before.

In another test, we repeated both the analyses with the `StORM` and `GYRE` grid with an altered χ^2 merit function in modelling step 3. We left the identified rotational splitting Δf_j out of the merit function, so the statistical parameter estimates are optimised to only the effective temperature $\log T_{\rm eff}$, luminosity $\log L$, and identified zonal mode frequencies $f_{0,j}$.

We first examine the impact of second-order rotation effects on the modelling of zonal modes by using the results found when neglecting the contributions of Δf_j in modelling step 3. Figure B.2 compares the largest discrepancy between the observed $f_{0,j}$ and the those in the model found with `StORM` and `GYRE`. Most stars lie well below the grey dotted line, which indicates that the model found with `StORM` grid outperforms the `GYRE` model. Therefore, we conclude that the treatment of rotationally induced stellar deformation included in `StORM` improves the fitting of $f_{0,j}$.

Next, Fig. B.3 compares the model quality with and without the contribution of Δf_j to χ^2 using the `StORM` grid. On one hand, the observed $f_{0,j}$ are generally better reproduced when Δf_j is not optimised alongside $f_{0,j}$ in β Cep stars rotating more

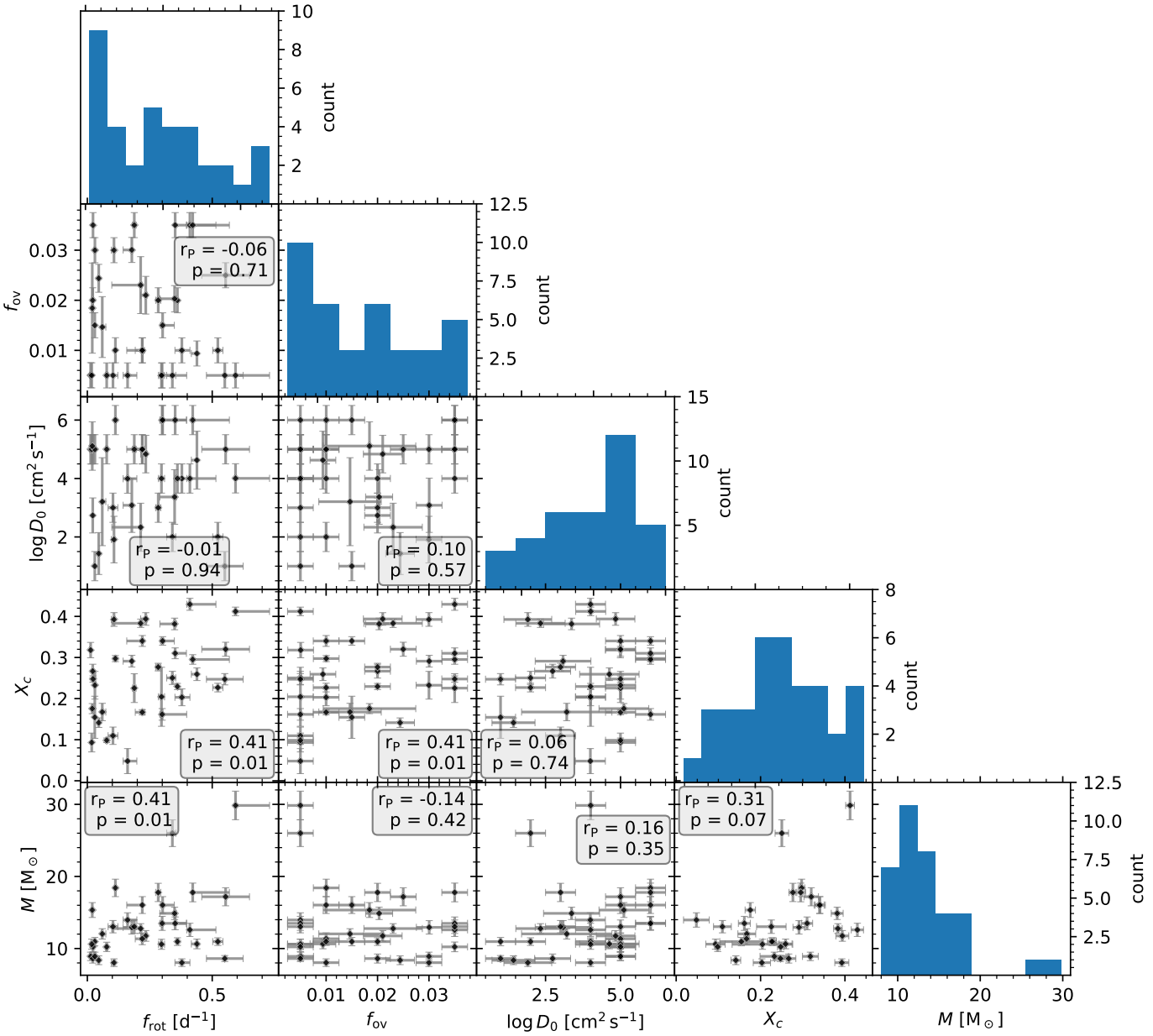

Fig. A.1: Corner plot of the rotation frequency, core overshoot parameter, envelope mixing strength, central hydrogen mass fraction and initial mass. Pearson correlation coefficients and p-values of the associated t-tests between each set of two parameters are included in boxes.

rapidly than 20% $f_{\rm crit}$. This indicates that beyond this rotation threshold, the difficulty in matching the observed rotational splitting may throw off the fitting of zonal frequencies. Figure B.4 shows two such stars, where one's model is weakly affected and the other's strongly affected by the change step 3. On the other hand, the observed dimensionless asymmetry and the mean rotational splitting $\overline{\Delta f}$ are naturally better reproduced when Δf_j is included. Notably, $\overline{\Delta f}$ is much better reproduced when including second-order effects at small $f_{\rm rot}/f_{\rm crit}$. These differences are exaggerated at small $f_{\rm rot}/f_{\rm crit}$ as $\overline{\Delta f}$ is reproduced precisely in both approaches, which makes the ratio between the two models volatile as the discrepancies in $\overline{\Delta f}$ are small. Nevertheless, this demonstrates that optimising asymmetric rotational splitting from second-order effects is still worthwhile even when $f_{\rm rot}$ is small, as also argued by Briquet et al. (2007). In summary, the inclusion of Δf_j in χ^2 can adversely affect the fitting of $f_{0,j}$ when $f_{\rm rot} > 20\%\, f_{\rm crit}$ and thus potentially throw off stellar parameters such as mass and age. However, it also leads to significantly better reproduction of non-zonal frequencies and thus produces a superior $f_{\rm rot}$ estimate at all rotation rates. Consequently, whether Δf_j should be optimised consistently depends the rotation regime as well as on which stellar parameters one prioritises.

To test how these different modelling approaches affect the derived stellar parameters, Fig. B.5 shows the five free parameters and the relative convective core mass $M_{\rm cc}/M$ obtained when including or excluding the Δf_j from χ^2. By and large, these modelling approaches produce similar results as the initial mass M and the central hydrogen mass fraction $X_{\rm c}$ as a proxy of age agree for most stars. Subsequently, $M_{\rm cc}/M$ is also in agreement.

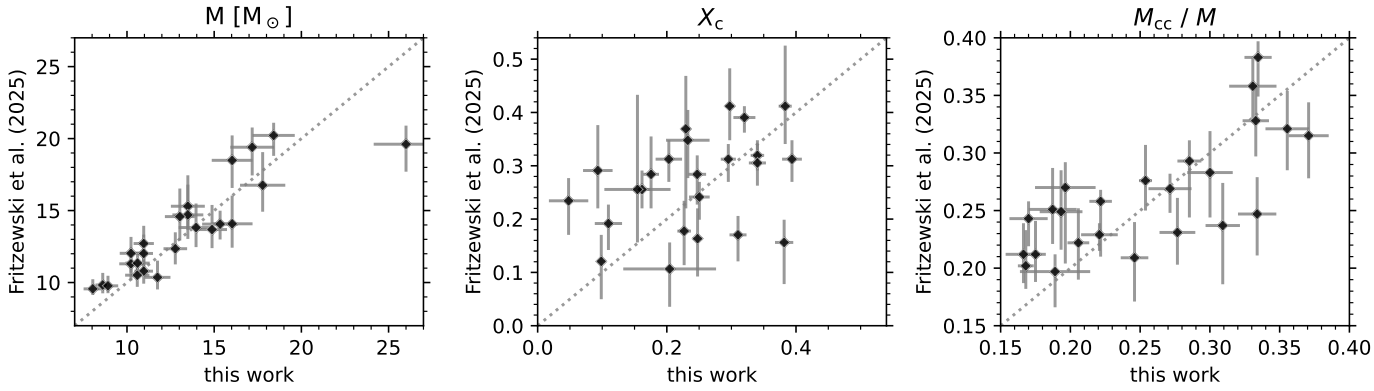

Fig. B.1: Comparison of the initial mass, central hydrogen mass fraction, and relative convective core mass from our modelling of 24 stars with the modelling by Fritzewski et al. (2025). The grey dotted lines indicate where the results from the two modelling procedures agree.

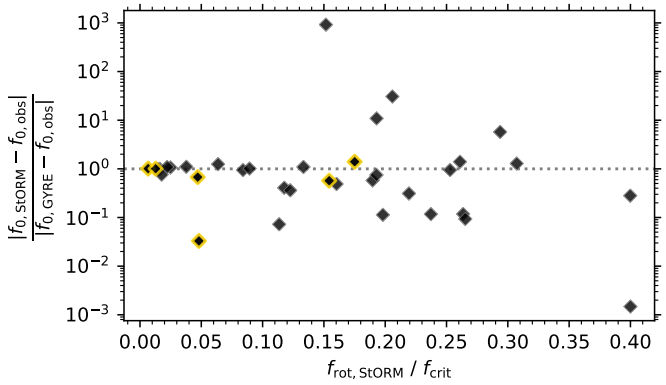

Fig. B.2: Ratio of the largest discrepancy in zonal frequency between the observations and models found with `StORM` over `GYRE` against the relative rotation frequency. The rotational splitting was not included in the χ^2 merit function in step 3. For stars below the grey dotted line, the modelling using `StORM` better reproduces the observed zonal modes than the modelling with `GYRE` and vice versa. The validation stars have a golden outline.

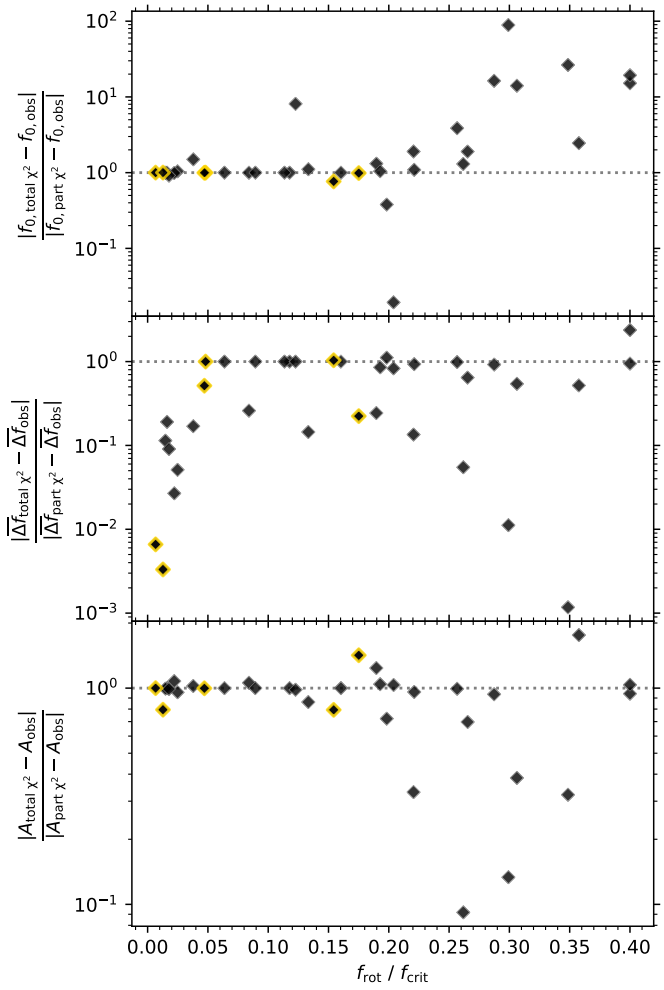

Fig. B.3: Ratio of the largest discrepancy between the observations and models when including over excluding the rotational splitting in χ^2 modelling step 3 against the relative rotation frequency. The top panel shows the discrepancies in zonal mode frequencies, the middle panel the mean splitting within a multiplet, and the bottom panel the dimensionless asymmetry parameter. For stars below the grey dotted line, the modelling with rotational splitting in χ^2 outperforms that without and vice versa. The validation stars have a golden outline.

Nonetheless, there are a handful of stars for which the two modelling procedures differ significantly as a different local minimum in χ^2 becomes the global minimum.

For completeness, we also compare the modelling results obtained with `StORM` and `GYRE` in Fig. B.6 with Δf_j considered in χ^2. Again, most parameters are broadly in agreement, although X_c tends to get underestimated when using `GYRE` at higher rotation rates as the reduction of mode frequencies due to stellar deformation is neglected. This results in significant differences in the estimates of the other parameters. Notably, these differences are larger than the scatter than in Fig. B.5, which suggests that the choice of oscillation code has a greater impact than some details of the modelling methodology. As also discussed in Sect. 5, the optimal f_{rot} is usually greater when using `GYRE` than when using `StORM`, especially at higher f_{rot}.

Appendix C: Sensitivity kernels

The low-radial order pulsations in β Cep stars typically have a broad rotational sensitivity kernel K_{nl}. Figure C.1 displays K_{nl}, calculated using equation (3.356) in Aerts et al. (2010),

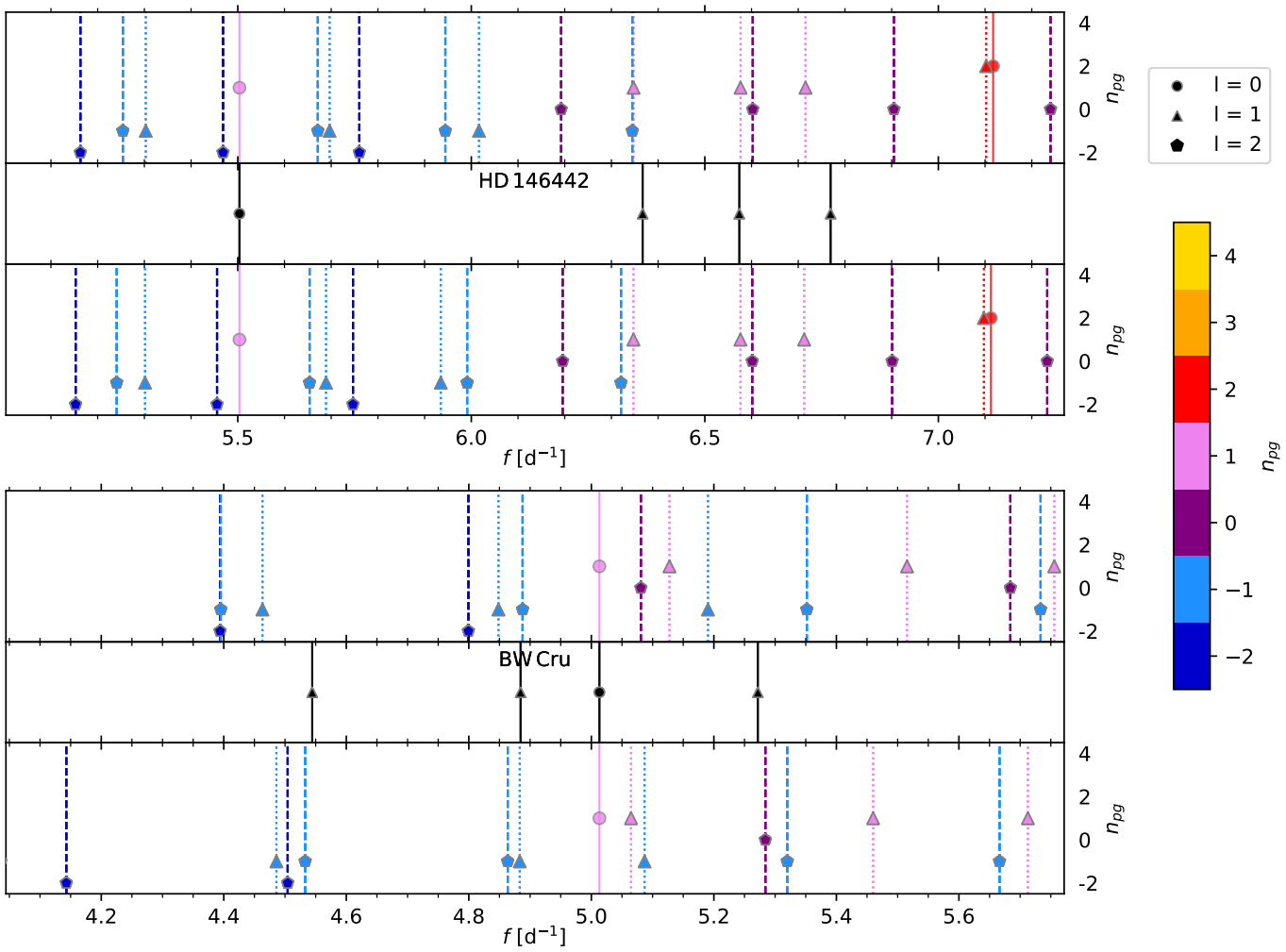

Fig. B.4: Idem Fig. 4, comparing two modelling approaches to observations for two example stars. For each example, three panels show the frequencies in the model found when including rotational splitting in the χ^2 merit function in modelling step 3 (top), the observations – neglecting amplitude for clarity – (middle), and the model found when excluding rotational splitting (bottom).

of the identified rotationally split multiplets in two stars. TIC 314833456 (top) has one multiplet sensitive to a thin region near the core and another sensitive to a broad part of the envelope, hence its core-to-envelope rotation ratio can be well constrained. Meanwhile, θ Oph has two multiplets that are both sensitive to approximately the same broad regions of the envelope. Consequently, these overlapping kernels average the rotation frequency over the same values, dampening the difference between the two measured rotation frequencies. Therefore, the constraint on the differential rotation in this star is merely a lower limit.

Appendix D: Electronic data, code, and figures

This paper is accompanied by a number of electronic tables containing all the observational constraints as well as all the modelling results required to reproduce the figures presented in the main text. Snippets of these tables are shown in this Appendix. Further instructions on how to access these electronic tables, electronic figures, and our forward modelling code are given in the Data Availability section above.

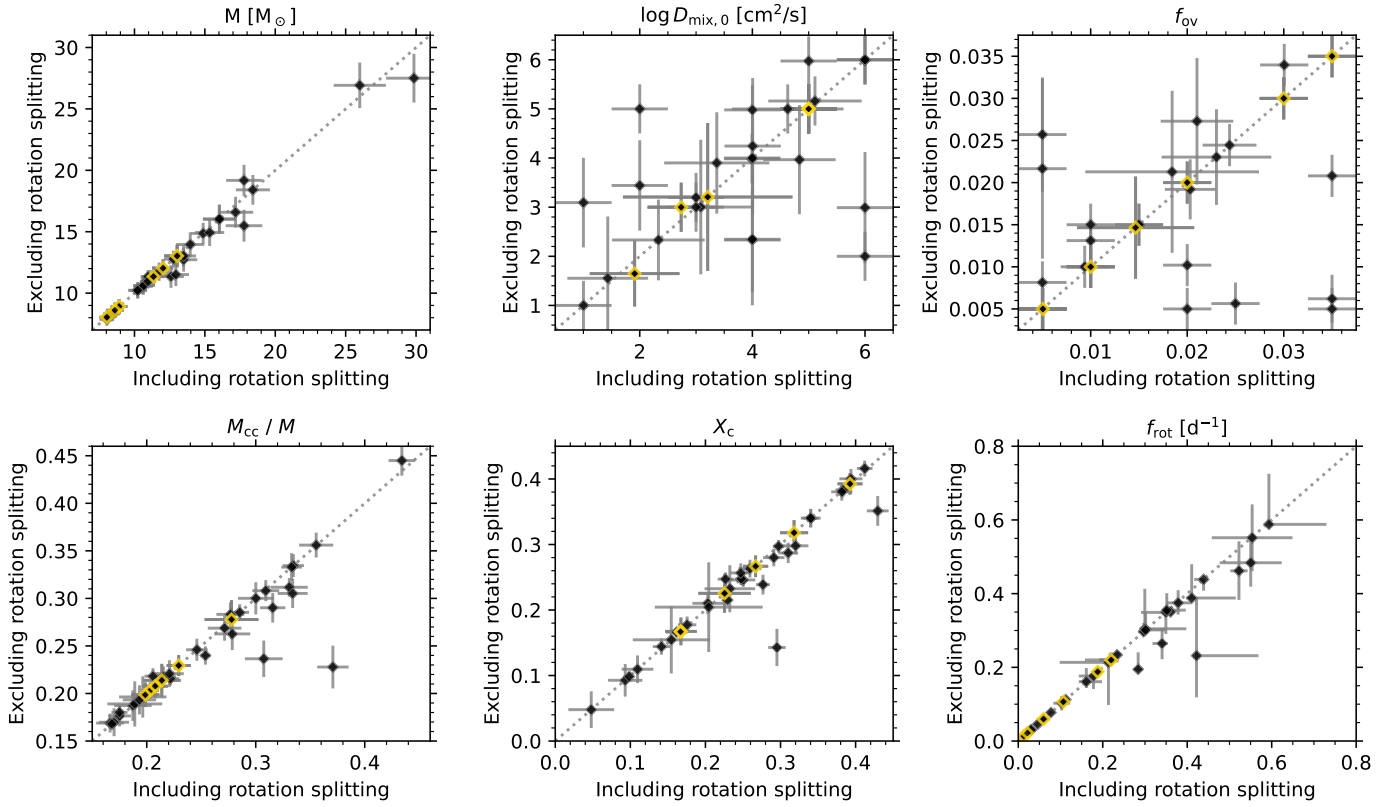

Fig. B.5: Comparison of the initial mass, mixing at the base of the envelope, core overshoot parameter, relative convective core mass, central hydrogen mass fraction, and rotation frequency found when including and excluding the rotational splitting in χ^2 in modelling step 3. Grey dotted lines indicate where the modelling results agree. The validation stars have a golden outline.

Table D.1: Observational input used in the modelling of five stars examined in this study, including mode identities. For simplicity, we omitted the uncertainties and the lists of all detected signals in this excerpt. Similarly, we only show one identified signal.

TIC ID	Name	*Gaia* DR3 ID	RA [°]	dec. [°]	V [mag]	success	source T_{eff}	log T_{eff} [K]	log L [L$_\odot$]	$f_{\mathrm{rot,surface}} \sin i$ [d^{-1}]	N_{i}	N_{f}	i_1	$n_{\mathrm{pg},1}$	l_1	m_1	f_1 [d^{-1}]	a_1
13332837	HD 229085	2061190956100233088	305.39636	38.61325	9.8	True	esphs	4.366	4.172	0.48	2	5	1	2	1	-1	8.638539	0.001555
14085632	TIC 14085632	2057943789022548096	305.72188	37.11278	11.0	True	esphs	4.533	4.938	0.38	2	7	1	1	1	-1	4.521608	0.003241
15166556	HD 146442	5990434159009246848	244.59709	-45.84034	9.11	True	esphs	4.362	3.727	0.76	2	4	1	1	1	-1	6.366871	0.002721
18827544	TIC 18827544	5941164183970835200	247.97767	-48.42875	12.28	False	esphs	4.398	3.939	0.38	2	4	1	…	1	-1	4.39127	0.000732
34590771	β CMa	-1	95.67494	-17.95592	1.97	True	Mazumdar2006	4.4	4.45	…	2	3	1	1	0	0	3.9995	2.6
…																		

Notes. N_{i} is the number of identified radial modes or rotationally split multiplets, i.e. how many unique sets of (n_{pg}, l) were identified, while N_{f} is the total number of identified modes observed. The columns suffixed with $_1$ describe the first identified pulsation mode. The complete table, including uncertainties, all identified frequencies, and lists of all detected frequencies including unidentified ones, is available at the CDS with additional documentation.

Table D.2: Modelling outcomes and statistical parameter estimation of five stars examined in this study when modelled using `StORM` and including rotational splitting in the merit function. For simplicity, we omitted the uncertainties in this excerpt.

TIC ID	Name	χ^2	$\lvert f_{0,obs} - f_{0,model} \rvert$ [d^{-1}]	M [M$_\odot$]	log $D_{\mathrm{mix},0}$ [cm^2 s]	f_{ov}	X_{c}	f_{rot} [d^{-1}]	$f_{\mathrm{rot}}/f_{\mathrm{crit}}$	age [Myr]	log T_{eff} [K]	log L [L$_\odot$]	log g [cm s^2]	log R [R$_\odot$]	M_{cc} [M$_\odot$]	M_{cc}/M
13332837	HD 229085	29658.7	8.2e-06	12.59	4.0	0.035	0.429	0.4106	0.2039	10.92	4.43	4.268	3.946	0.796	3.87	0.307
14085632	TIC 14085632	317.2	0.006026	18.41	6.0	0.01	0.297	0.1123	0.084	7.74	4.477	4.798	3.765	0.968	6.16	0.335
15166556	HD 146442	1844.8	0.002667	8.04	4.0	0.01	0.203	0.3785	0.2211	29.56	4.295	3.702	3.775	0.784	1.34	0.166
34590771	β CMa	0.8	4.87e-05	12.03	3.2	0.0147	0.167	0.0598	0.0481	15.67	4.37	4.306	3.644	0.936	2.57	0.214
42940133	HD 228101	184.4	0.0013233	11.75	4.8	0.021	0.394	0.234	0.1177	12.56	4.411	4.183	3.926	0.791	3.25	0.277
…																

Notes. The full table, including uncertainties, is available at the CDS with additional documentation. Similar tables using the alternative modelling methods described in Appendix B.2 are also available at the CDS.

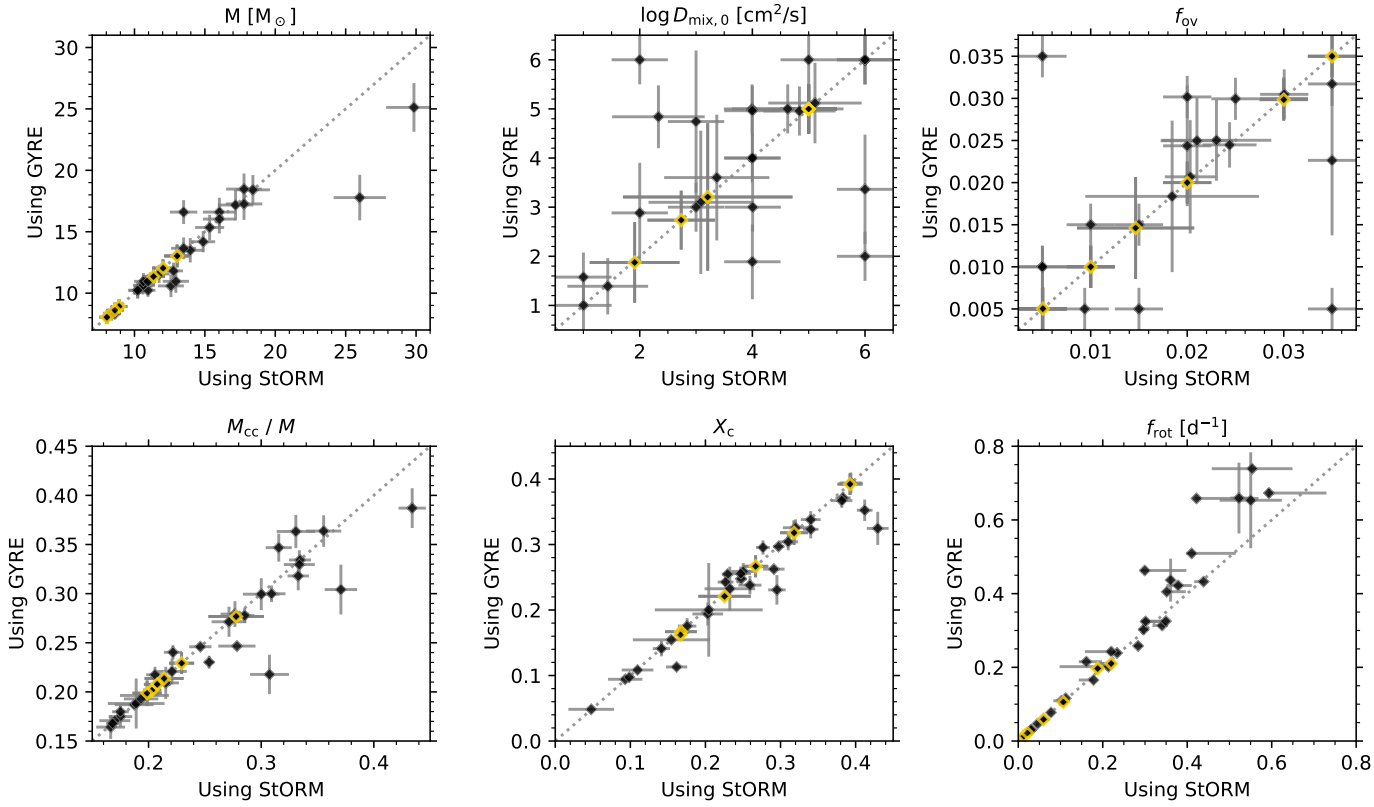

Fig. B.6: Comparison of the initial mass, mixing at the base of the envelope, core overshoot parameter, relative convective core mass, central hydrogen mass fraction, and rotation frequency found from `StORM` and `GYRE`. Grey dotted lines indicate where the modelling results agree. The validation stars have a golden outline.

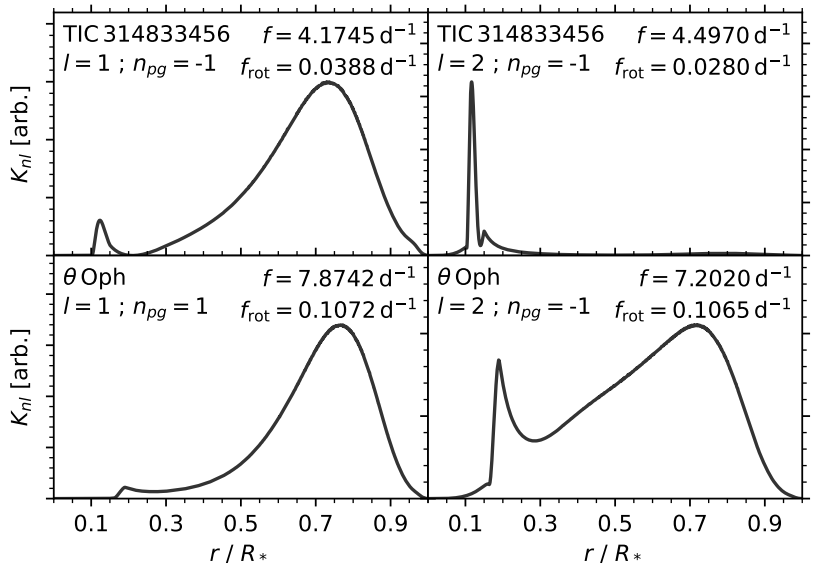

Fig. C.1. Sensitivity kernels of each identified rotationally split multiplet in the β Cep stars TIC 314833456 and θ Oph. In each panel, we include the name of the star and the multiplet's degree, radial order, zonal frequency, and extracted rotation frequency.

Table D.3: Observed and modelled rotational splitting in each identified multiplet of five stars in our sample.

TIC ID	Name	n_{pg}	l	$f_{0,\mathrm{obs}}$ [d^{-1}]	$f_{0,\mathrm{model}}$ [d^{-1}]	$\Delta f_{1,\mathrm{obs}}$ [d^{-1}]	$\Delta f_{-1,\mathrm{obs}}$ [d^{-1}]	$\Delta f_{2,\mathrm{obs}}$ [d^{-1}]	$\Delta f_{-2,\mathrm{obs}}$ [d^{-1}]	$A_{1,\mathrm{obs}}$	$A_{2,\mathrm{obs}}$	$\Delta f_{1,\mathrm{model}}$ [d^{-1}]	$\Delta f_{-1,\mathrm{model}}$ [d^{-1}]	$\Delta f_{2,\mathrm{model}}$ [d^{-1}]	$\Delta f_{-2,\mathrm{model}}$ [d^{-1}]	$A_{1,\mathrm{model}}$	$A_{2,\mathrm{model}}$	f_{rot} [d^{-1}]	$\sigma_{f_{\mathrm{rot}},-}$ [d^{-1}]	$\sigma_{f_{\mathrm{rot}},+}$ [d^{-1}]	$f_{\mathrm{rot,GYRE}}$ [d^{-1}]	C_{nl}
13332837	HD 229085	2	1	9.13184	9.13184	0.59119	0.4933	…	…	-0.09026	…	0.25463	0.55531	…	…	0.37123	…	0.4174	0.0007	0.1636	0.5656	0.04127
13332837	HD 229085	1	1	6.87714	6.87715	…	0.3861	…	…	…	…	0.26675	0.38614	…	…	0.18286	…	0.3838	0.029	0.029	0.402	0.03959
14085632	TIC 14085632	1	1	4.63305	4.63305	0.1386	0.11144	…	…	-0.10864	…	0.108	0.13197	…	…	0.09988	…	0.1275	0.0009	0.027	0.133	0.06005
14085632	TIC 14085632	-1	2	4.21651	4.21048	0.09717	0.07341	…	0.15961	-0.13931	…	0.07823	0.08066	0.15343	0.16478	0.01527	0.03569	0.1047	0.0007	0.0056	0.1129	0.24158
15166556	HD 146442	1	1	6.57384	6.57651	0.19547	0.20697	…	…	0.02857	…	0.13906	0.22906	…	…	0.24449	…	0.3785	0.0045	0.0323	0.4165	0.51682
15166556	HD 146442	1	0	5.50359	5.50359	…	…	…	…	…	…	…	…	…	…	…	…	…	…	…	…	…
34590771	β CMa	1	0	3.9995	3.9995	…	…	…	…	…	…	…	…	…	…	…	…	…	…	…	…	…
34590771	β CMa	-2	2	3.8828	3.88275	…	…	0.0965	…	…	…	0.04861	0.04934	0.0965	0.09949	0.00746	0.01529	0.0598	0.0016	0.0016	0.0589	0.18062
42940133	HD 228101	0	2	7.1674	7.16607	0.22259	0.24275	…	0.43567	0.04331	…	0.21416	0.2214	0.42089	0.44987	0.01662	0.03328	0.234	0.0023	0.0023	0.235	0.0661
42940133	HD 228101	1	0	6.30245	6.30245	…	…	…	…	…	…	…	…	…	…	…	…	…	…	…	…	…
…																						

Notes. Each row in this table represents one rotationally split multiplet or radial mode, meaning there are several rows per star. We included the statistical rotation frequency estimate from our modelling step 3, its asymmetric uncertainties, and the rotation frequency found with the simplified 'a posteriori' step from the Ledoux constant estimated with `GYRE`. In the subscripts of rotational splitting $\Delta f_{m,\mathrm{source}}$ and dimensionless asymmetry parameter $A_{|m|,\mathrm{source}}$, 'm' indicates the azimuthal order and 'source' whether the value comes from the observations or the best model. The zonal frequencies $f_{0,\mathrm{source}}$ use the same scheme. The full table is available at the CDS with additional documentation.

Table D.4: The constraints on differential rotation in five stars in our sample. We only show the rotation and kernel positions from one rotationally split multiplet in this excerpt for brevity.

TIC ID	Name	$f_{\mathrm{rot,surface}} \sin i$ [d^{-1}]	$\sigma_{f_{\mathrm{rot,surface}} \sin i}$ [d^{-1}]	f_{rot} [d^{-1}]	$\sigma_{f_{\mathrm{rot}},-}$ [d^{-1}]	$\sigma_{f_{\mathrm{rot}},+}$ [d^{-1}]	X_{c}	$\sigma_{X_{\mathrm{c}}}$	N_{r}	$f_{0,1}$ [d^{-1}]	n_1	l_1	$f_{\mathrm{rot},1}$ [d^{-1}]	$\sigma_{f_{\mathrm{rot},1},-}$ [d^{-1}]	$\sigma_{f_{\mathrm{rot},1},+}$ [d^{-1}]	$(r/R_*)_{\mathrm{mode},1}$	$(r/R_*)_{\mathrm{mean},1}$	$(r/R_*)_{\mathrm{median},1}$
13332837	HD 229085	0.48	0.15	0.4106	0.0125	0.1043	0.429	0.015	2	9.13184	2	1	0.4174	0.0007	0.1636	0.882	0.738	0.837
14085632	TIC 14085632	0.38	0.10	0.1123	0.0034	0.0019	0.297	0.007	2	4.63305	1	1	0.1275	0.0009	0.027	0.744	0.431	0.437
15166556	HD 146442	0.76	0.23	0.3785	0.0278	0.0323	0.203	0.02	1	6.57384	1	1	0.3785	0.0045	0.0323	0.131	0.451	0.196
34590771	β CMa	…	…	0.0598	0.0043	0.0143	0.167	0.021	1	3.8828	-2	2	0.0598	0.0016	0.0016	0.123	0.406	0.384
42940133	HD 228101	0.46	0.12	0.234	0.0204	0.005	0.394	0.015	1	7.1674	0	2	0.234	0.0023	0.0023	0.205	0.405	0.265
…																		

Notes. N_r is the number of identified rotationally split multiplet. The columns $(r/R_*)_{\mathrm{X}}$ are the relative radius of the position of the maximum, mean and median of the sensitivity kernel. The columns suffixed with $_1$ describe the first identified multiplet. The full table, including all identified rotationally split multiplets, is available at the CDS with additional documentation.